AGU PUBLICATIONS

JGR

Journal of Geophysical Research: Atmospheres

RESEARCH ARTICLE
10.1002/2016JD025690

Special Section:
Deep Convective Clouds and Chemistry 2012 Studies (DC3)

An overview of the 29 May 2012 Kingfisher supercell during DC3

E. A. DiGangi[1,2], D. R. MacGorman[2], C. L. Ziegler[2], D. Betten[3], M. Biggerstaff[3], M. Bowlan[3], and C. K. Potvin[1,2,3]

[1]Cooperative Institute for Mesoscale Meteorological Studies, University of Oklahoma, Norman, Oklahoma, USA, [2]NOAA/National Severe Storms Laboratory, Norman, Oklahoma, USA, [3]School of Meteorology, University of Oklahoma, Norman, Oklahoma, USA

Key Points:
- DC3 acquired a comprehensive suite of observations addressing all of its goals from the 29 May 2012 DC3 supercell case analyzed here
- This overview of the storm's kinematics, microphysics, and lightning provides essential context for studies by other DC3 investigators
- The kinematic and microphysical properties derived from mobile radar observations are consistent with the noninductive charge mechanism

Correspondence to:
E. A. DiGangi,
elizabeth.digangi@noaa.gov

Citation:
DiGangi, E. A., D. R. MacGorman, C. L. Ziegler, D. Betten, M. Biggerstaff, M. Bowlan, and C. K. Potvin (2016), An overview of the 29 May 2012 Kingfisher supercell during DC3, *J. Geophys. Res. Atmos.*, *121*, 14,316–14,343, doi:10.1002/2016JD025690.

Received 25 JUL 2016
Accepted 9 NOV 2016
Accepted article online 14 NOV 2016
Published online 20 DEC 2016

Abstract On 29–30 May 2012, the Deep Convective Clouds and Chemistry experiment observed a supercell thunderstorm on the southern end of a broken line of severe storms in Oklahoma. This study focuses on an approximately 70 min period during which three mobile Doppler radars operated and a balloon-borne electric field meter, radiosonde, and particle imager flew through the storm. An overview of the relationships among flash rates, very high frequency (VHF) source densities, and Doppler-radar-derived storm parameters is presented. Furthermore, the evolution of the flash distribution relative to the midlevel storm's kinematics and microphysics is examined at two times during a period of rapid storm intensification. The timing of increases in VHF counts in the 8–10 km above ground level (agl) layer, which contained the largest VHF source counts, is similar to the timing of increases in updraft mass flux, in updraft volume, and in graupel volume at approximately 5–9 km agl. Although some increases in VHF source counts had little or no corresponding increase in one or more of the other storm parameters, at least one other parameter had an increase near the time of every VHF increase, a pattern which suggests a common dependence on updraft pulses, as expected from the noninductive graupel-ice electrification mechanism. A classic bounded weak lightning region was observed initially during storm intensification, but late in the period it appeared to be due to a wake in the flow around the updraft, rather than due to a precipitation cascade around the updraft core as is usually observed.

1. Introduction

The Deep Convective Clouds and Chemistry (DC3) field experiment was conducted during May–June of 2012 in three domains: northern Alabama, Oklahoma/west Texas, and Colorado. The goals of DC3 were to investigate the production of NO_x by lightning, the transport of NO_x, and other species by convective-scale motions to the upper troposphere, the longer-term photochemistry of sunlight acting on the species in the upper troposphere, and the relationships between lightning and internal thunderstorm processes [*Barth et al.*, 2015]. Storms in all three domains were sampled by instrumented aircraft, mobile Doppler radars, the National Weather Service Weather Surveillance Radar–'88 Doppler (WSR-88D) network, and Lightning Mapping Arrays (LMAs), and soundings were obtained in the storm environments. Storms targeted in the OK/TX domain also were sampled by in situ weather balloons carrying particle imagers, electric field meters, and radiosondes.

The 29 May Kingfisher supercell storm was the southernmost cell in a broken line of five severe storms in north-central OK chosen for intensive analysis by DC3 investigators. The far inflow and upper tropospheric outflow of the Kingfisher storm were sampled by multiple instrumented aircraft [*Barth et al.*, 2015], three soundings were launched in the near-storm inflow environment, three mobile radars sampled the storm simultaneously for over an hour, and a ground support crew launched two in situ balloon soundings. The storm was also within range of the Oklahoma Lightning Mapping Array (OK-LMA), thus facilitating the collection of high-resolution total lightning data for the storm's entire lifetime. Although a discussion of the Kingfisher storm's charge structure is outside the scope of this study, *DiGangi* [2014] found that the vertical polarity of the storm's overall charge distribution was inverted from the usual polarity [e.g., *MacGorman et al.*, 2005], with upper level storm charge being negative instead of positive and midlevel charge being positive instead of negative. During the period of DC3 field operations, the storm intensified, producing total flash rates $>100\,\mathrm{min}^{-1}$ and vertical vorticities exceeding $30\times10^{-3}\,\mathrm{s}^{-1}$. The storm continued to intensify after aircraft operations ended, producing flash rates exceeding $400\,\mathrm{min}^{-1}$, hail up to 12 cm

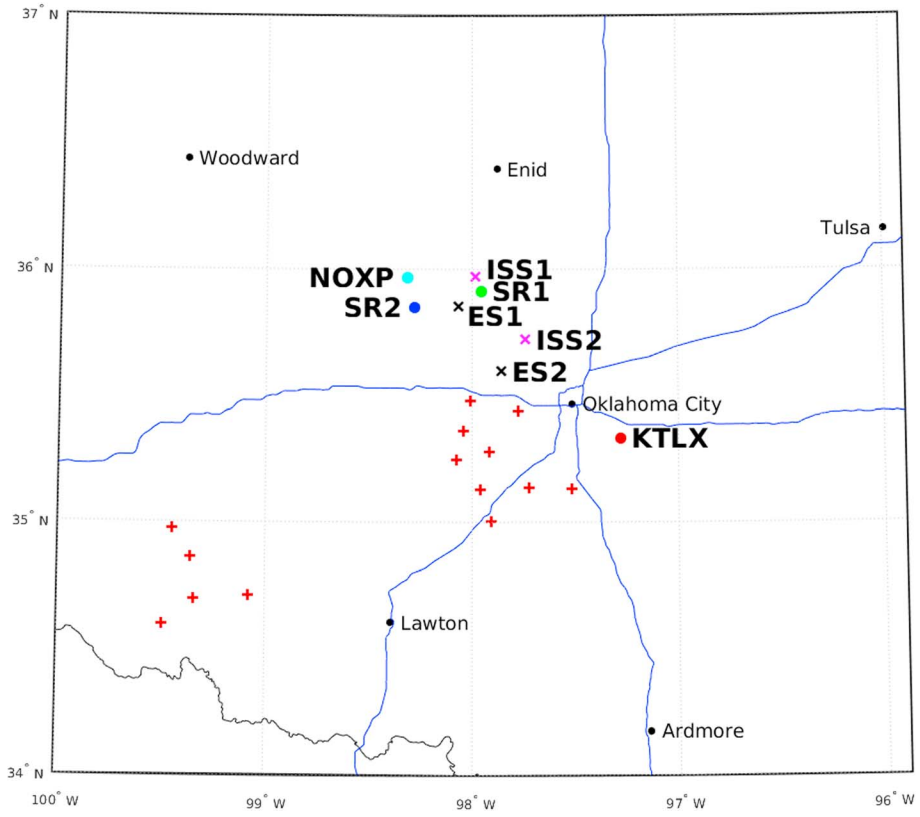

Figure 1. Map depicting the locations of the active OK LMA stations (red crosses), the deployed mobile radars (SR1, SR2, and NOXP), the Oklahoma City operational WSR-88D radar (KTLX), and the in-storm (ISS1 and ISS2) and environmental (ES1 and ES2) sounding launch sites.

(5 inch) in diameter, and a weak EF-1 tornado. The wealth of data collected for this case made it an excellent candidate for study.

The purpose of this paper is to provide an overview of the evolution of severe weather reports and of various radar, lightning, and microphysical parameters of the Kingfisher storm, including some novel aspects of the behavior of total lightning activity. Although some information is presented about the whole lifetime of the storm, our analysis focuses on the period of mobile radar observations during DC3's field operations. Besides providing information about the evolving relationships between lightning and other storm properties (a primary goal of DC3), the observations and analysis in this study also provide much of the storm context needed both in follow-on studies and by other DC3 investigators studying various aspects of this case.

2. Data and Methodology

This study incorporates observational data from several platforms: radar reflectivity from the WSR-88D network; mobile soundings of the near-storm environment [*Ziegler*, 2013c]; reflectivity, 3-D wind retrievals, and other parameters from three mobile radars [*Biggerstaff*, 2014a, 2014b; *Mansell*, 2014]; and lightning parameters derived from the OK-LMA [*MacGorman*, 2013]. Various microphysical parameters were retrieved by a diabatic Lagrangian analysis [*Ziegler*, 2013a, 2013b] using a combination of the time-dependent mobile radar analyses and environmental soundings. Figure 1 shows the locations of all observing systems used in this study, as well as the locations of the in-storm balloon soundings, which collected radiosonde, particle imager [*Waugh et al*., 2015], and electric field meter (EFM) data. The imager data are not presented here because they form the basis of a detailed study of the microphysics inferred from radar and observed by the imager in a recently completed doctoral research project [*Waugh*, 2016] and are intended for a future journal paper. EFM data from one launch were compared with the storm charge distribution inferred from LMA observations by *DiGangi* [2014] and will be included in another follow-on study. The instrumented aircraft sampled

Table 1. List of Mobile Dual-Doppler Pairs Chosen From the SR1, SR2, and NOXP Radar Observations as Applied to Obtain the 3 min Interval Variational Dual-Doppler Wind Synthesis of the 29 May 2012 Kingfisher Storm[a]

Time Period (UTC)	Radar Pairs	Comment
2251–2257	SR1-NOXP	Pure dual-Doppler
2300–0000	SR1-NOXP	Dual-Doppler pair yielding optimal
	SR1-SR2	Viewing geometry applied at any
	SR2-NOXP	Given grid point location

[a]The mobile radar locations (Figure 1) have radar pair baseline lengths of 14.25 km (SR2-NOXP), 19 km (SR1-SR2), and 30 km (SR1-NOXP). The resulting time-spaced analyses are dual-Doppler at any given grid point location, although the 3-D synthesis employs observations from two to three radars depending on analysis time period.

the near-storm environment, which is not a focus of this study, and the anvil region outside the dual-Doppler domain of this study. Some aircraft data from this case have already been analyzed in other DC3 studies [e.g., *Barth et al*., 2016].

2.1. Radar Observations

Mobile radar data were collected by the Shared Mobile Atmospheric Research and Teaching Radars (SMART-Radar or "SR") SR1 and SR2 [*Biggerstaff et al*., 2005] and the National Oceanic and Atmospheric Administration National Severe Storms Laboratory (NSSL) X-band polarimetric radar [*Burgess et al*., 2010]. Time-synchronized radar volume scans were obtained at a 3 min interval by two to three radars from 2251 UTC on 29 May to 0000 UTC on 30 May 2012 (all times are universal time unless noted otherwise).

A sequence of dual-Doppler radar wind syntheses were performed using the variational (VAR) method described by *Potvin et al*. [2012] utilizing optimal radar pairs as summarized in Table 1. The VAR wind syntheses all employed a nearby environmental sounding to provide the background field for each synthesis, which was then blended smoothly with in-storm winds using a low-pass spatial filter. Each radar volume scan was interpolated to a Cartesian grid using natural neighbor interpolation [*Ledoux and Gold*, 2005]. The analysis domain was 90 km (west-east) × 60 km (south-north) × 17.5 km (altitude above ground level (agl)) with horizontal and vertical grid spacing of 500 m and the first analysis level at 200 m agl.

Data from the WSR-88D [*Crum and Alberty*, 1993] radar KTLX provided observations of the Kingfisher storm over the course of its entire lifetime. KTLX had yet not received its scheduled dual-polarimetric upgrade as of May 2012, so only reflectivity and radial velocity data were available for WSR-88D analysis. These data were obtained from the National Climatic Data Center archive and displayed in the Warning Decision Support System–Integrated Information (WDSS-II) software platform [*Lakshmanan et al*., 2007].

2.2. Lightning

The OK-LMA uses technology developed by New Mexico Tech [*Rison et al*., 1999; *Krehbiel et al*., 2000; *Thomas et al*., 2004]. It consists of a ground-based network of stations located in central and southwestern Oklahoma, each of which detects the very high frequency (VHF) radiation emitted by lightning channel segments as a flash develops [*MacGorman et al*., 2008]. A single lightning flash can emit tens to thousands of VHF signals, and the OK-LMA uses a time-of-arrival technique to determine the time and 3-D location (latitude, longitude, and altitude) of the source of any signal within 100 km of the network center from the different times at which the signal arrives at the stations [*Rison et al*., 1999; *MacGorman et al*., 2008]. VHF source position errors within this range are estimated to be 10 m in the horizontal, 30 m in the vertical, and 40 ns in time [*Thomas et al*., 2004; *Lund et al*., 2009]. The location errors increase with range beyond the perimeter of stations but are typically much less than 1 km within the region analyzed in the present study. Details concerning the equipment, data processing, and time and location errors in LMAs are described by *Rison et al*. [1999] and *Thomas et al*. [2004].

To be considered reliable enough for the present study, a VHF source was required to be detected by at least seven stations, the reduced chi-square of the source computation less than 2, and the source height below 20 km, as in previous studies [e.g., *MacGorman et al*., 2008; *Lund et al*., 2009; *Weiss et al*., 2012; *Calhoun et al*., 2013]. To simplify subsequent procedures, all VHF sources outside the subjectively drawn boundaries of the Kingfisher storm were withheld from the LMA analyses. Cloud-to-ground (CG) flashes were identified with data from the National Lightning Detection Network (NLDN) [*Cummins and Murphy*, 2009].

The Kingfisher storm became increasingly difficult to isolate after 0000 (approximately halfway through the storm's lifetime) as additional storms formed or moved into its vicinity, although the uncertainties in delineating the subject storm fortunately had little effect on the number of flashes or flash rate trends [*DiGangi*, 2014]. The effect on flash rates was much larger as a left-moving supercell storm originating in southern Oklahoma

began merging with the Kingfisher storm late in its lifetime. Lightning from the merging left-moving storm was included in the analyzed data set after the two storms were indistinguishable from each other in the LMA data. The merger period is noted on all figures generated with these data.

The "clean" LMA data were processed via the algorithms "w2lmaingest" and "w2lmaflash" in WDSS-II. Algorithm w2lmaingest ingests LMA data and converts it to a format usable by the WDSS-II platform. Algorithm w2lmaflash takes the ingested LMA data, groups the sources into flashes, and calculates an array of products, including flash extent density and flash initiation locations [*Herzog*, 2013]. The criteria for adding a VHF source to a flash were based on the time ($<$150 ms) and distance ($<$3 km) to previous sources in the flash. To be used in flash products, a flash was required to be composed of at least 10 VHF sources, both to eliminate single-source discharges (which typically are numerous and would skew statistics) and to provide enough sources to compute robust flash initiation locations. Each flash initiation location was calculated as described by *Lund et al*. [2009] to determine its latitude, longitude, and altitude and was assigned the time of the first point in the flash. The 1 min total flash rate was then calculated by summing the number of flash initiations for each minute of the storm's lifetime.

To calculate the horizontal distribution of lightning, the code package "lmatools" was utilized. The lmatools code sorts VHF sources into flashes in the same way as w2lmaflash but also requires flashes to have a horizontal dimension of at least 0.15 km. The lmatools code then derives multiple parameters and maps them onto a 2-D grid. For this study, we analyzed the number of flashes that were initiated within each grid column and the total number of flashes passing through a grid column (i.e., flash extent density or FED). The grid stencil used with lmatools coincided with the grid points of the more spatially limited dual-Doppler radar synthesis and diabatic Lagrangian analysis (DLA) grid domain (sections 2.1 and 2.3, respectively), thus facilitating the direct overlay of lmatools output fields on the radar and Lagrangian analyses. The storm boundaries for these comparative gridded analyses typically excluded a significant portion of the downstream forward anvil region and, at times, included parts of a second supercell storm to the north of the Kingfisher storm.

Although the gridded lightning data were vertically integrated and projected on a 2-D grid, they can nevertheless usefully be overlaid on plots at various altitudes of parameters from the radar and Lagrangian analyses. FED and flash initiations were computed from 10 min of lightning data centered on each analysis time ($\pm$5 min). A period of 6 min was tested, but trends in the data were clearer with 10 min intervals. The FED grid was smoothed by replacing the value of each grid cell with the arithmetic average of that cell and the eight cells surrounding it. A given grid cell was omitted from the smoothing process if it did not contain any VHF sources, thereby preventing the smoothing code from spreading data into adjacent grid cells where no lightning was observed.

In addition to OK-LMA observations, data from the NLDN [*Stossmeister*, 2012] were used to determine what fraction of the total flash count were cloud-to-ground (CG) flashes. To identify which CG flashes were associated with the Kingfisher storm, plots of NLDN ground strike points were compared with plots of flashes in the clean OK-LMA data set.

2.3. Diabatic Lagrangian Analysis

A diabatic Lagrangian analysis (DLA) has been applied to the 29 May storm with an updated version of the methods discussed by *Ziegler* [2013a] (hereafter referred to as Z13) and *Ziegler* [2013b]. Predicted 3-D cloud ice and diagnosed snow mixing ratio fields have recently been added to the DLA, as described in the Appendix A. The enhanced DLA algorithm first calculates the field of upstream parcel trajectories from each DLA grid point via the time-dependent airflow described in section 2.1 by extending the trajectory backward in time into the storm's inflow environment. Environmental sounding data are interpolated to determine the potential temperature θ (K), the water vapor mixing ratio q_v (g/kg), and the ambient total pressure (mb) at the initial Lagrangian point. The Lagrangian algorithm then integrates a system of first-order ordinary differential equations forward in time for each trajectory from its initial point in the environment to its ending DLA grid point [Z13]. The algorithm interpolates the reflectivity to each Lagrangian point along a trajectory during integration and diagnoses the time-varying Lagrangian values of rainwater mixing ratio q_r (g/kg), snow mixing ratio q_s (g/kg), and graupel/hail mixing ratio q_g (g/kg) for subsequent microphysical and thermodynamic Lagrangian calculations. The predicted Lagrangian variables are θ, q_v, cloud water mixing ratio q_c (g/kg), and cloud ice mixing ratio q_x (g/kg).

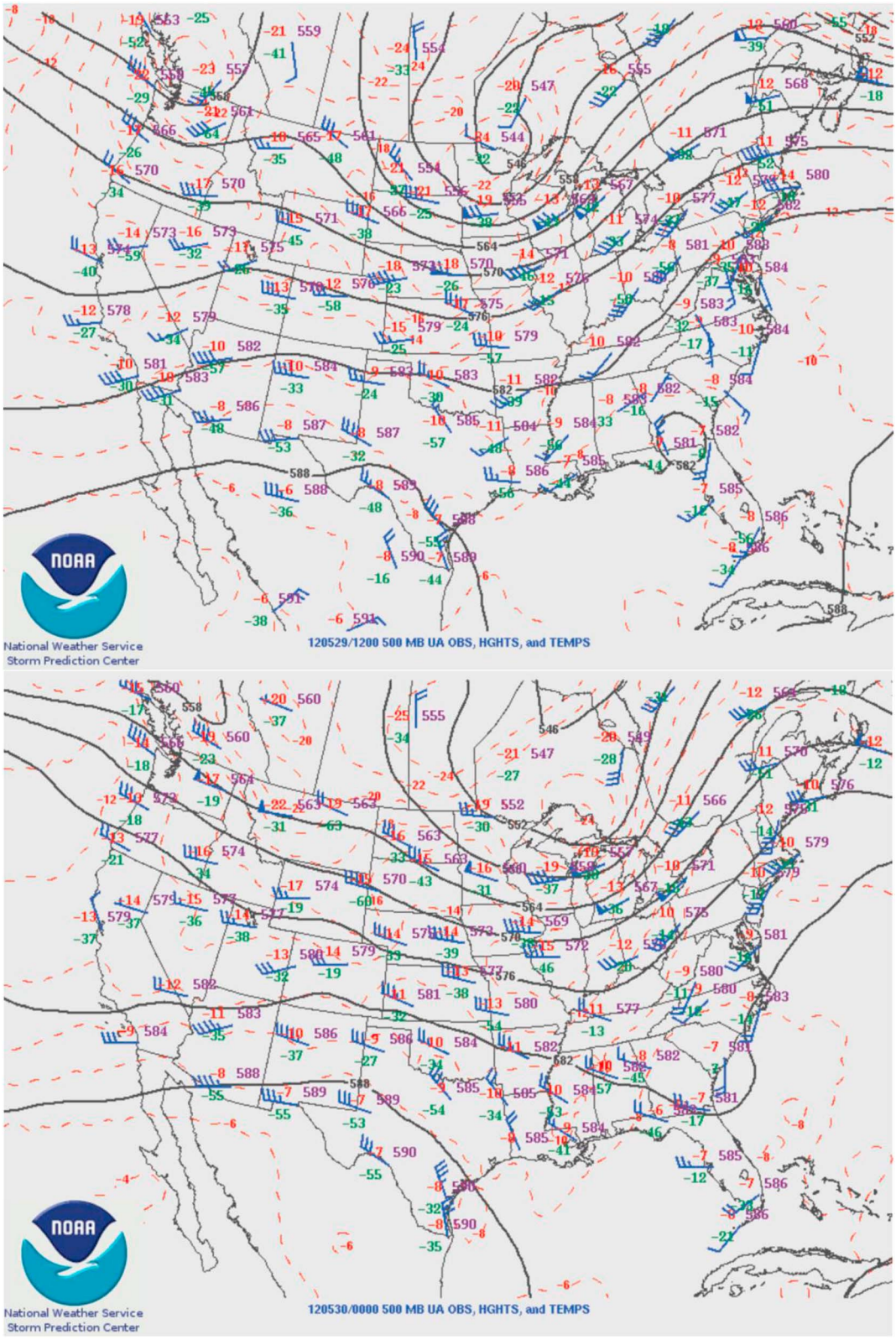

Figure 2. The 500 mb analyses from the Storm Prediction Center (SPC) archive for (a) 29 May at 12:00 UTC and (b) 30 May at 00:00 UTC.

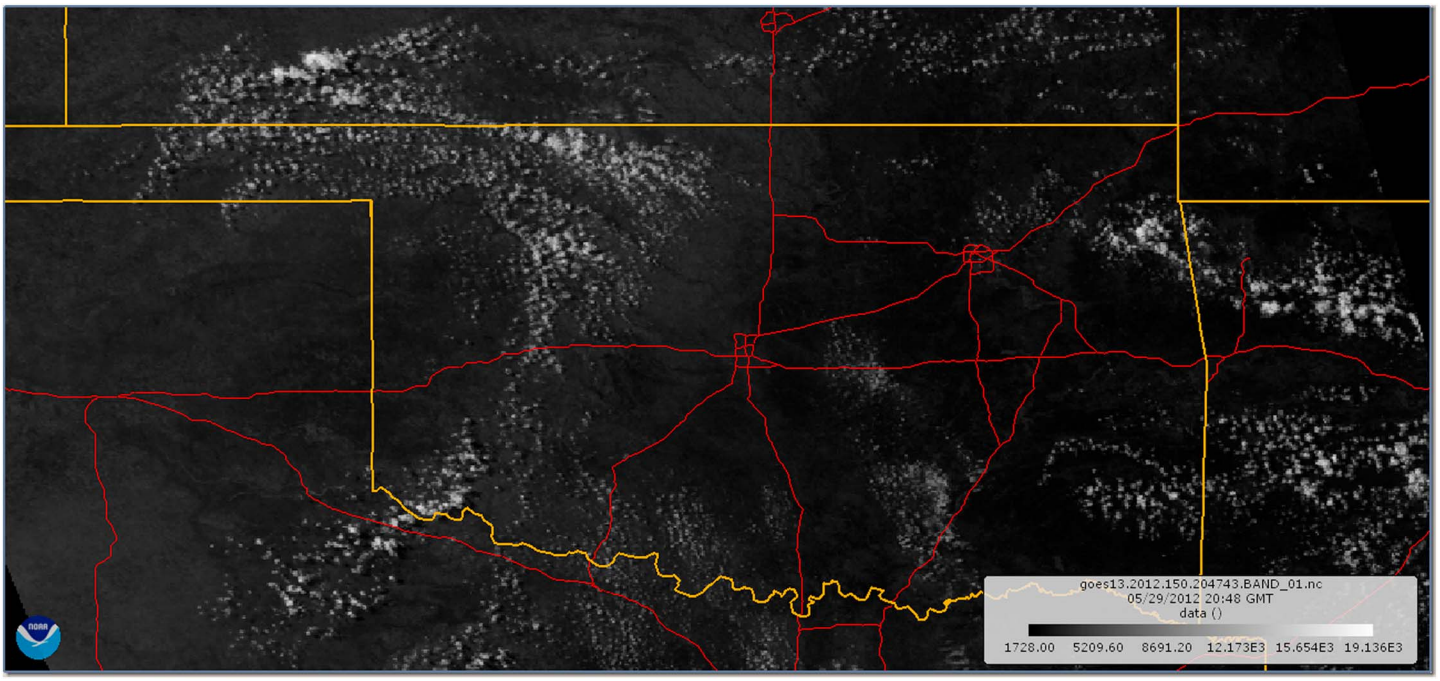

Figure 3. GOES-13 visible imagery of Oklahoma at 2048 UTC on 29 May 2012.

2.4. Storm Reports

Reports of severe weather events for this case were obtained from the Storm Data archive [*National Climatic Data Center*, 2012]. Because these reports originate from the general public, the data set contains inherent uncertainty. However, it is the most comprehensive and readily available data set of hail and tornado occurrence [*Herzog*, 2013]. This study compares the timing of hail and tornado reports for the Kingfisher storm with the trends observed in the radar, lightning, and DLA analyses.

3. Storm Environment

The large-scale pattern on 29 May 2012 was characterized by an open wave over south-central Canada, which caused rebounding midlevel height rises over Oklahoma and Kansas, the region of interest of the present study. The regional flow at 500 mb was nearly zonal, with minor diffluence over Oklahoma and Kansas (Figure 2). A short-wave trough was over the Oklahoma panhandle, and a low-pressure center had developed in the Texas panhandle. A stationary front extended from this low eastward into southern Kansas, and a dryline arced southward from the low to the Big Bend region of the Texas-Mexico border (Figures 3 and 4).

The 1200 sounding from Norman, Oklahoma, on 29 May 2012 (not shown) was very strongly capped with little to no convective available potential energy (CAPE). Convection initiation (CI) around 2120 near Fairview in north-central Oklahoma was associated with development of the first storm to the east of the dryline bulge and south of the stationary front where a vigorous cumulus field was visible before 2100 (not shown). A mobile sounding launched in the near-storm environment at 2255 contained a mixed-layer CAPE ("MLCAPE") of 2372 J kg^{-1}, a 0–3 km storm-relative helicity ("SRH0-3") of 271 m^2 s^{-2}, a bulk speed shear in the lowest 6 km ("SHR0-6") of 24 m s^{-1}, and a nearly dry-adiabatic midlevel lapse rate (Figure 5a). There was a small residual cap in place to help keep storms mostly isolated from one another. Low-level veering, broadly unidirectional middle and upper tropospheric flow, and moderate bulk speed shear combined with large MLCAPE values provided strong support for both splitting and right-moving supercells. The mobile environmental sounding at 0020 (Figure 5b) provided stronger support for rotating supercells due to a combination of increased vapor mixing ratio and directional shear in the boundary layer (BL), with MLCAPE and SRH0-3 both increasing substantially to 3010 J kg^{-1} and 463 m^2 s^{-2}, respectively, in comparison to the 2255 sounding.

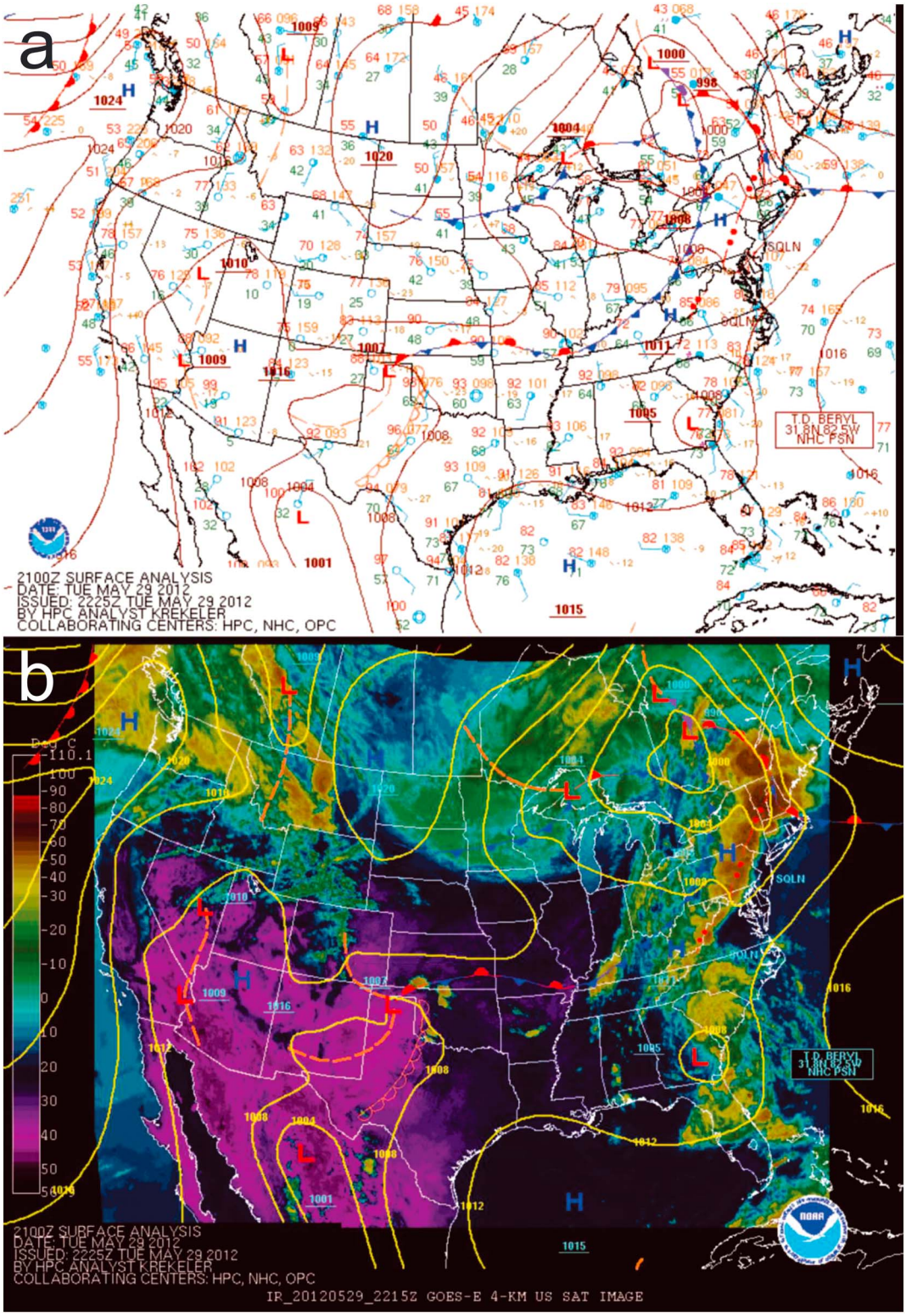

Figure 4. Surface analyses from the Hydrometeorological Prediction Center (HPC) archive, with overlaid (a) ground observations at 22:25 UTC and (b) infrared satellite imagery at 22:15 UTC.

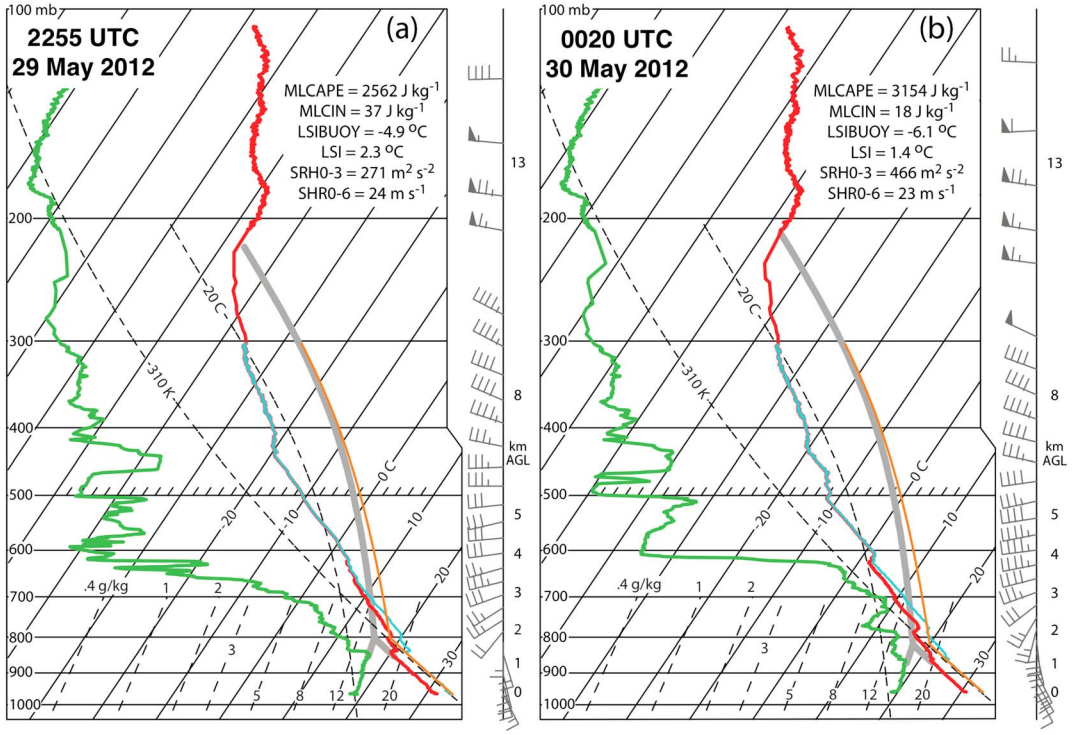

Figure 5. Mobile environmental soundings launched in the upstream inflow of the Kingfisher storm on 29–30 May 2012 (located as in Figure 1) at the following times: (a) 2255 and (b) 0020. Two critical parameters used in the diabatic Lagrangian analysis are the ambient environmental melting level (~4.1 km agl) and the −15°C level in the moist-adiabatic main updraft (~7.7 km). The freezing level in the moist-adiabatic updraft is at ~5.2 km. An estimated motion (m s^{-1}) of (u, v) = (7, −3) for the Kingfisher storm was used to calculate SRH0-3.

4. Storm Overview

Low-elevation angle KTLX observations reveal that the first reflectivity echoes of the southernmost convective cell appeared at 2104 (1604 CDT; Figure 6), the northernmost cell appeared in the next volume scan (at 2113), and sustained deep convection (i.e., CI as described by *Kain et al*. [2013]) was observed by around 2120. The two storms moved slowly east-northeastward, but both expanded and developed a low-level reflectivity maximum >50 dBZ within 30 min after CI. The northern cell intensified more quickly than the southern storm and began producing lightning just after 2120. The first detected lightning in the southern storm occurred at 2134.

Persistent midlevel mesocyclonic radial velocity signatures were visible in both storms by 2200 (not shown), thereby marking their transition to the supercell phase [e.g., *Bunkers et al*., 2006]. The southern storm split between 2200 and 2230, and the right mover (henceforth referred to as the Kingfisher storm) subsequently began moving southeastward while maintaining its mesocyclone (Figure 6). The left mover was absorbed into new convection just north of the Kingfisher storm. The new convection and the northern storm both then split, and the new left mover merged with the northern storm's right mover. A line of four supercell storms had thus formed in northwest Oklahoma by 2300, the Kingfisher storm being the southernmost cell. During the initial split of the southern storm, total flash rates of the Kingfisher storm increased to greater than 50 flashes min^{-1}, but after 2230 the total flash rates decreased to under 10 flashes min^{-1} (Figure 7). Hail ranging from 3.8 to 5.1 cm (1.5–2 inch) in diameter was reported from the Kingfisher storm following the initial split (Figure 8).

The Kingfisher storm began intensifying after 2300 as the total flash rate steadily increased (Figure 7), and isolated VHF sources began occurring in the overshooting top above 13 km agl (Figure 9). VHF sources occurred continually throughout the duration and volume of the overshooting top during each overshooting top episode, as is characteristic of discharges in this region, in sharp contrast to the bursts of VHF sources typically lasting less than 1 s comprising flashes within the main body of the

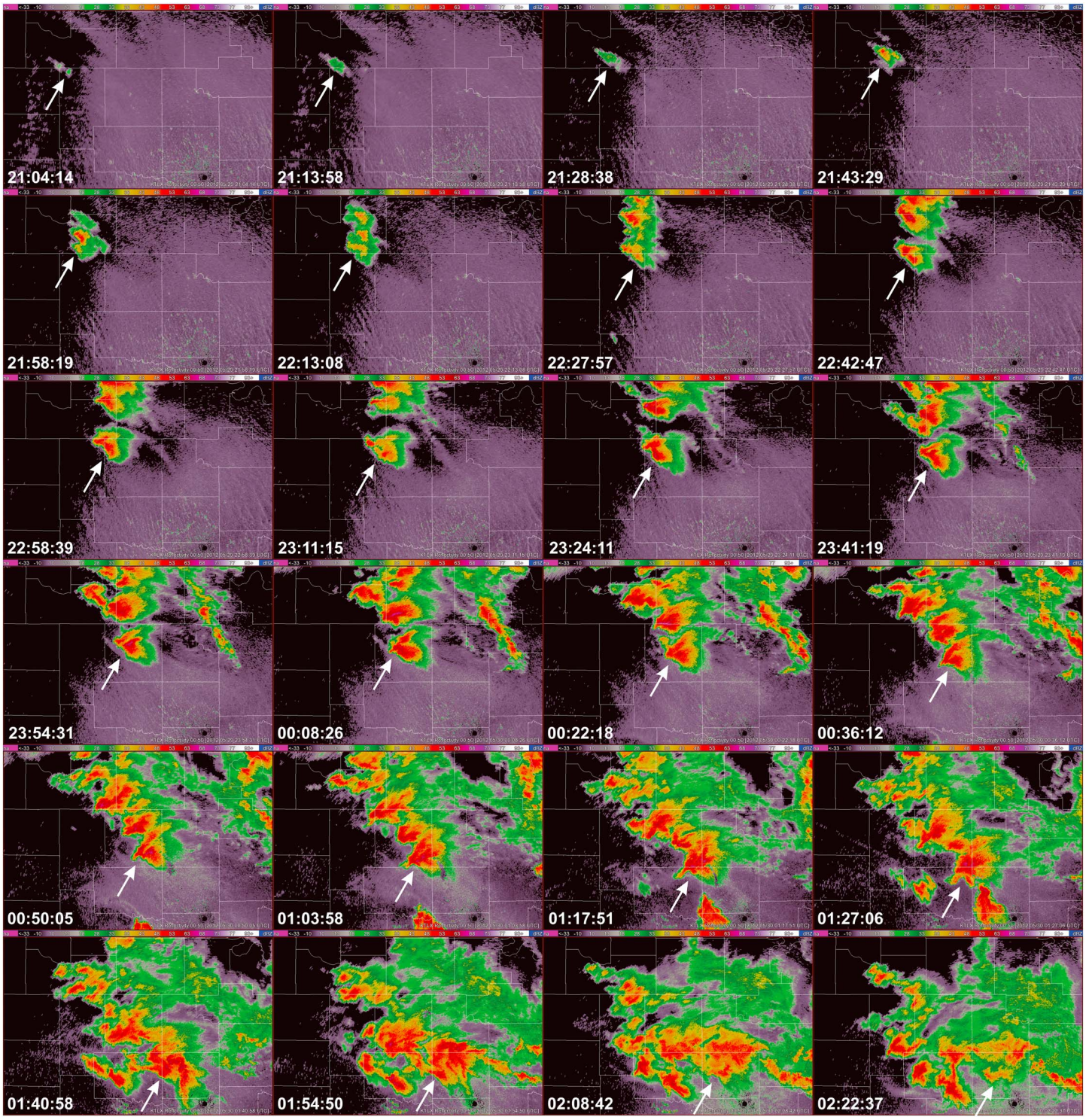

Figure 6. KTLX radar reflectivity mosaic depicting the storm complex sampled on 29–30 May 2012, including the Kingfisher storm, from 2104 to 0222. The locations of the Kingfisher storm are indicated before 0140, and the locations of the merged storm are indicated after 0140.

Kingfisher storm [*Calhoun et al.*, 2013; *Elliott*, 2013]. The discharges above the equilibrium level pulsed in height and duration as the overshooting top itself pulsed, in response to pulses in the storm's updraft, and were maintained more steadily as reflectivity in overshooting tops was maintained more steadily after 0000.

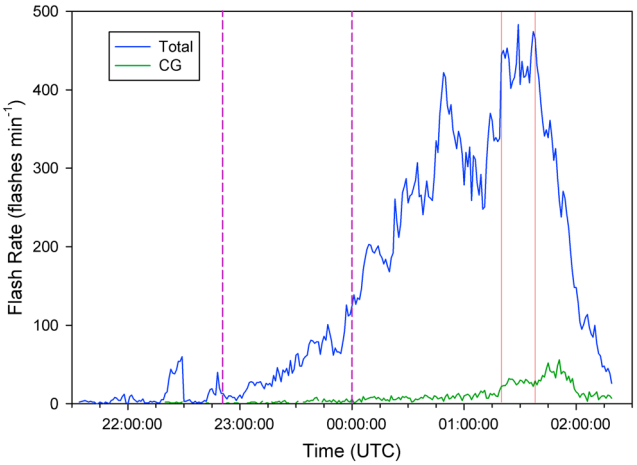

Figure 7. Total and cloud-to-ground flash rates for the Kingfisher storm throughout its lifetime. The vertical purple dashed lines indicate the multi-Doppler analysis period, while the vertical red lines indicate the merger period.

New deep convection began forming both to the west of the existing storms and to the east beneath the merged downshear anvils between 2325 and 0000 (Figure 6). The formation of lightning-containing secondary convection in the forward overhang Kingfisher storm anvil is in itself of significant interest (but outside the scope of the present study) and is the subject of a follow-on study. The initial secondary anvil convection eventually propagated rapidly eastward and later merged with the line of supercell storms to form a mesoscale convective system.

Total flash rates in the Kingfisher storm increased rapidly after 0000, peaking at 422 flashes min^{-1} shortly before 0100 and subsequently maintaining around 300 flashes min^{-1} for over 30 min (Figure 7). The storm maintained its supercellular structure, although a right mover that had split from the storm immediately north of the Kingfisher storm partially merged with the northern flank of the Kingfisher storm beginning around 0030 (Figure 6). Several occurrences of severe hail were reported during this period (Figure 8).

A left-moving supercell which had propagated northward from near the Oklahoma-Texas border began merging with the Kingfisher storm by around 0120 (Figure 6), when lightning in the upper levels of the two storms increasingly overlapped. Total flash rates in the Kingfisher storm had increased to greater than 300 min^{-1} before the merger (Figure 7) as giant hail up to 12.7 cm (5 inch) in diameter was reported in northeastern Oklahoma City (Figure 8). The total flash rate peaked at 483 flashes min^{-1} during the merger (Figure 7), although an indeterminate fraction of this increase could possibly be an artifact caused by the impulsive combination of both storms' flashes. The merger process lasted about 18 min, with its completion being defined as that time at which the reflectivity signatures of the two storms were completely joined at the lowest elevation angle [e.g., *Westcott and Kennedy*, 1989].

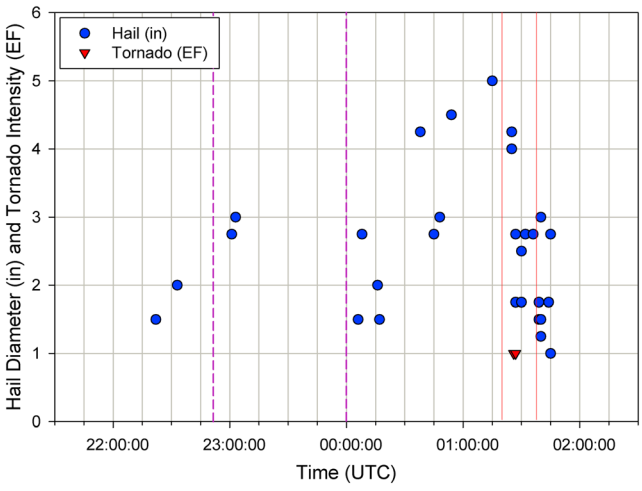

Figure 8. Severe weather reports for the Kingfisher storm throughout its lifetime. The key at the top left denotes the symbols for hail and tornado reports. The vertical purple dashed lines indicate the multi-Doppler analysis period, while the vertical red lines indicate the merger period.

The merged storm remained strong for a short time but quickly began to decay and merge with other storms around it. This was reflected by a rapid decrease in total flash rates from over 450 flashes min^{-1} during the merger to under 100 flashes min^{-1} about 30 min after the merger ended. Although the total flash rate decreased during this time, the CG flash rates actually increased briefly before decreasing again as the storm dissipated (e.g., Figure 7). The merged Kingfisher storm produced no more lightning after 0220, by which time it had almost completely dissipated in low-level reflectivity displays. Its remnants and

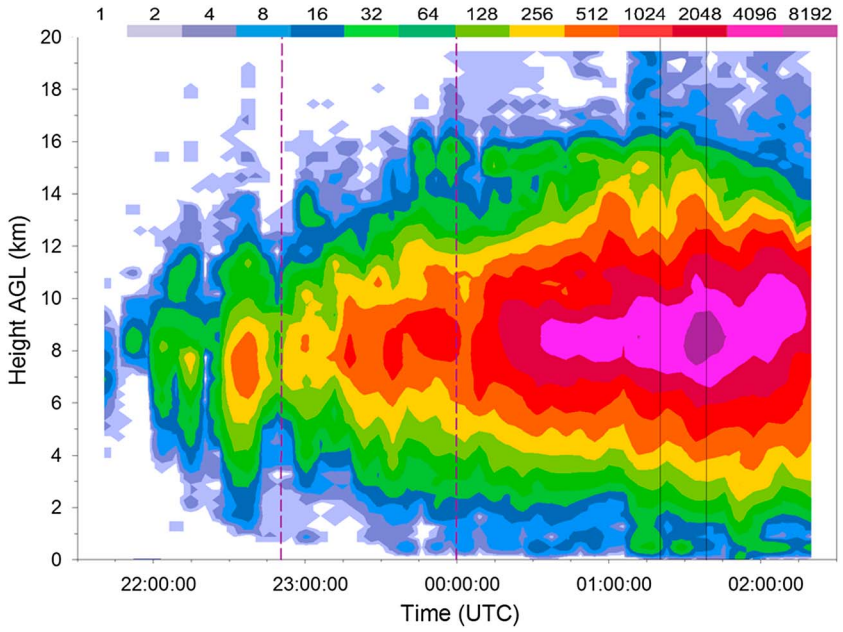

Figure 9. Time-height plot of lightning VHF source densities (# (500 m)$^{-1}$) for the storm lifetime. The vertical purple dashed lines indicate the multi-Doppler analysis period, while the vertical black lines indicate the merger period.

other storms in the vicinity continued merging together and eventually formed a mesoscale convective system, which propagated SE out of the Oklahoma City metropolitan area.

5. Dual-Doppler Analysis Period

5.1. Time Series Analyses

The time series of dual-Doppler mobile radar wind syntheses and Lagrangian analyses revealed the intensification phase of the Kingfisher storm from 2251 to 0000. The storm was characterized by increasing total flash rates and generally matching increases of updraft mass flux and volume and the volume and integrated mass of graupel/hail during this period (Figure 10). This implied general correlation between the kinematics, microphysics, and electrification in the mixed-phase updraft charging region has been rather well established based on several previous observational and storm simulation studies [*Deierling and Petersen*, 2008; *Calhoun et al.*, 2013; *Carey and Rutledge*, 1996; *Wiens et al.*, 2005; *Kuhlman et al.*, 2006; *Tessendorf et al.*, 2007]. Time-

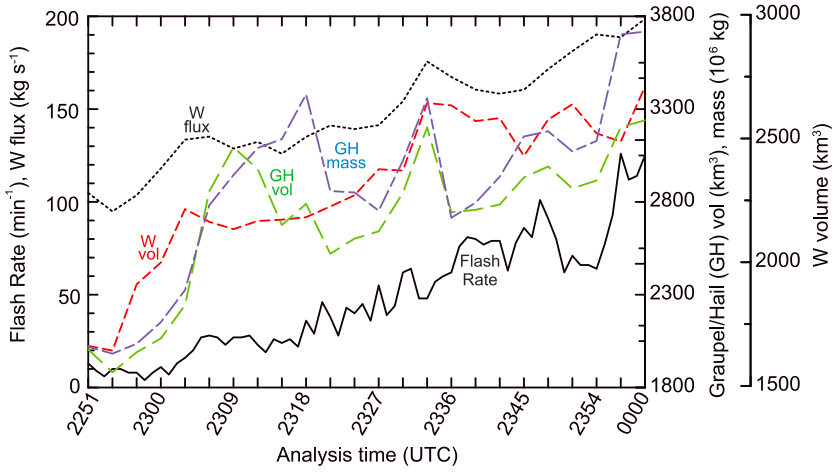

Figure 10. Time series of the total flash rates, updraft mass flux, and the integrated volume and mass of graupel/hail at subfreezing temperatures in the Kingfisher storm during the multi-Doppler analysis period.

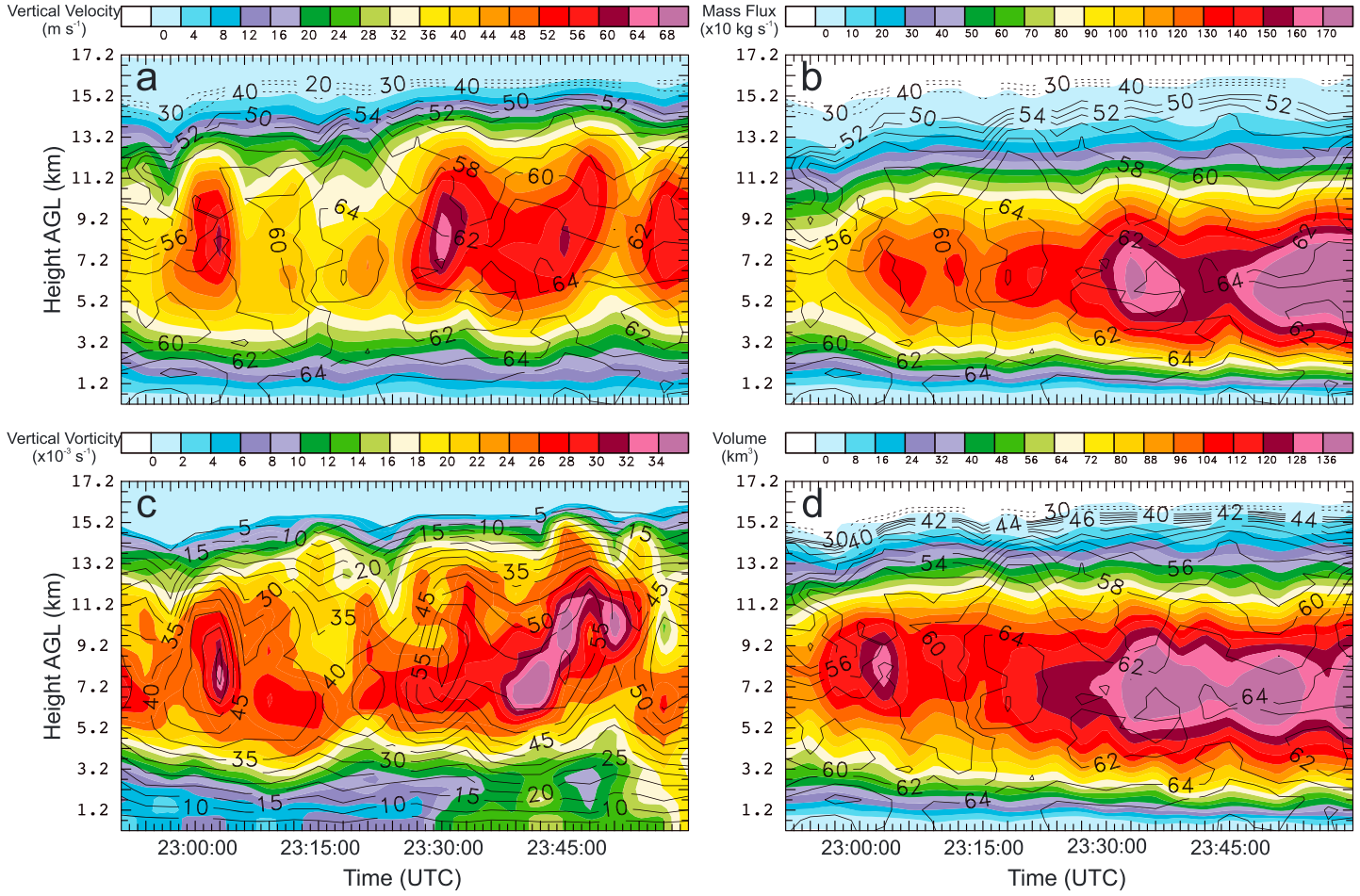

Figure 11. Time-height plots of multiple-Doppler derived fields for the Kingfisher storm: (a) color-filled maximum updraft with contours of maximum reflectivity (dB*Z*), (b) color-filled updraft mass flux with contours of maximum reflectivity, (c) color-filled maximum vertical vorticity with contours of maximum updraft ($m\,s^{-1}$), and (d) color-filled updraft volume with contours of maximum reflectivity. The horizontally integrated updraft volume is the summed number of grid cells having an updraft $>3\,m\,s^{-1}$ in a particular layer times the grid cell volume. The horizontally integrated updraft mass flux is the summation of the product of updraft speed times the density of air at that altitude times the grid cell area times the number of grid cells with $w > 3\,m\,s^{-1}$. Major tickmarks on the horizontal axis are at 3 min intervals indicating the time-spaced radar analysis times.

height analyses indicate that the updraft and reflectivity cores exceeding $20\,m\,s^{-1}$ and 50 dB*Z*, respectively, pulsed upward at approximately 2302, 2318, 2330, 2348, and around the end of the analysis period at 0000 (Figure 11a). Although the updraft mass flux and volume (Figures 11b and 11d) increased at middle levels of the storm during each pulse, the latter increases tended to occur a few minutes later than the increases in maximum updraft speed and to extend longer in time. The time lag of updraft mass flux relative to updraft speed was probably forced by growth in the horizontal area of the updraft, which in turn was slower to develop than maximum updraft speeds. These comparative trends of updraft mass flux and volume relative to peak updraft are consistent with supercell storm simulations which obtain smoother, more sensitive increases of overall areal- or volume-integrated storm intensity relative to point maximum updraft values, which tend to rather rapidly saturate around a fixed fractional value of the maximum updraft from parcel theory [e.g., *Ziegler et al.*, 2010].

Some parameters associated with the updraft pulses varied more erratically, even in the time-height plots. For example, maximum updraft speeds exceeded $60\,m\,s^{-1}$ in three of the four pulses, and speeds exceeding $50\,m\,s^{-1}$ extended to increasing heights in the third and fourth pulses but not in the second pulse (Figure 11a). On the other hand, the second pulse (which contained the weakest maximum updraft speeds with no maxima exceeding $48\,m\,s^{-1}$) achieved the greatest depth and duration of reflectivities exceeding 64 dB*Z* (Figure 11a). Throughout the analyzed period, vertical vorticity (Figure 11c) exceeded $20 \times 10^{-3}\,s^{-1}$

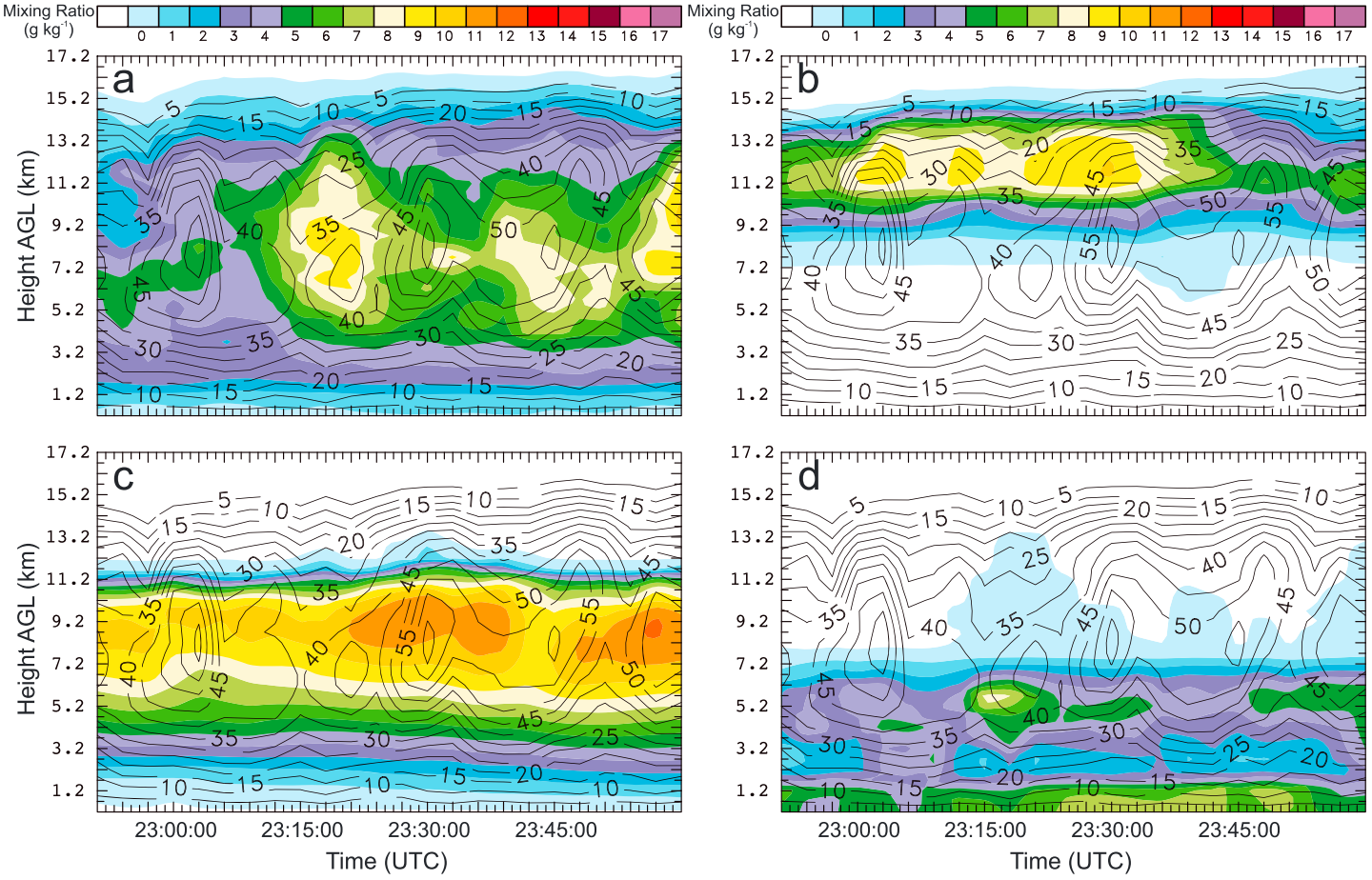

Figure 12. Time-height plots of contoured maximum updraft speed ($m\,s^{-1}$) superimposed on color-shaded DLA microphysical parameters: (a) graupel/hail maximum mixing ratio ($g\,kg^{-1}$), (b) cloud ice maximum mixing ratio ($g\,kg^{-1}$), (c) cloud water maximum mixing ratio ($g\,kg^{-1}$), and (d) rainwater maximum mixing ratio ($g\,kg^{-1}$). Major tickmarks on the horizontal axis are at 3 min intervals indicating the time-spaced radar analysis and DLA times.

somewhere in the storm in relation to minimal mesocyclone strength defined as $10\times10^{-3}\,s^{-1}$ [*Brandes*, 1984]. However, the maximum vertical vorticity had declined to less than $30\times10^{-3}\,s^{-1}$ after the first pulse and did not reach that threshold again until the fourth pulse, which had the greatest duration and height of vertical vorticity exceeding $30\times10^{-3}\,s^{-1}$ as the storm began taking on a more clearly defined supercell structure (not shown). The low-level (i.e., lowest 1 km layer) mesocyclone did not achieve minimal intensity until after 2329 (Figure 11c), interestingly initiating within and growing upward from the BL before subsequently intensifying downward from midlevels.

Variations in the aforementioned updraft characteristics influenced the microphysical development of the Kingfisher storm as inferred from the DLA (Figures 12 and 13). For example, the timing of larger values of graupel/hail mixing ratio exceeding $7\,g\,kg^{-1}$ (Figure 12a) associated with reflectivities exceeding 62 dB*Z* (Figure 11a) was most similar to that of updraft mass flux (Figure 11b). The timing of larger values of cloud ice mixing ratio (Figure 12b) at around 12 km and cloud water mixing ratio (Figure 12c) around 9 km after 2320 were similar to maxima of updraft mass flux (Figure 11b) and updraft volume (Figure 11d) due to fluctuating cloud condensation and freezing in the main updraft. It is also noted that broadly large values of maximum graupel/hail mixing ratio (Figure 12a) were consistent with a sustained deep region of large supercooled cloud contents (Figures 12c and 13c), owing to the known predominance of graupel/hail growth by collection and freezing of supercooled cloud droplets [e.g., *Heymsfield et al.*, 1980; *Ziegler et al.*, 1983; *Ziegler*, 1988]. Similarly, at midlevels of the storm, the timing of larger values of graupel/hail mixing ratio (Figure 12a) and graupel/hail volume (Figure 13a) was similar to that of updraft volume (Figure 11d). Rain mixing ratio in a small volume (Figure 13d) containing highly localized large peak mixing ratios exceeding

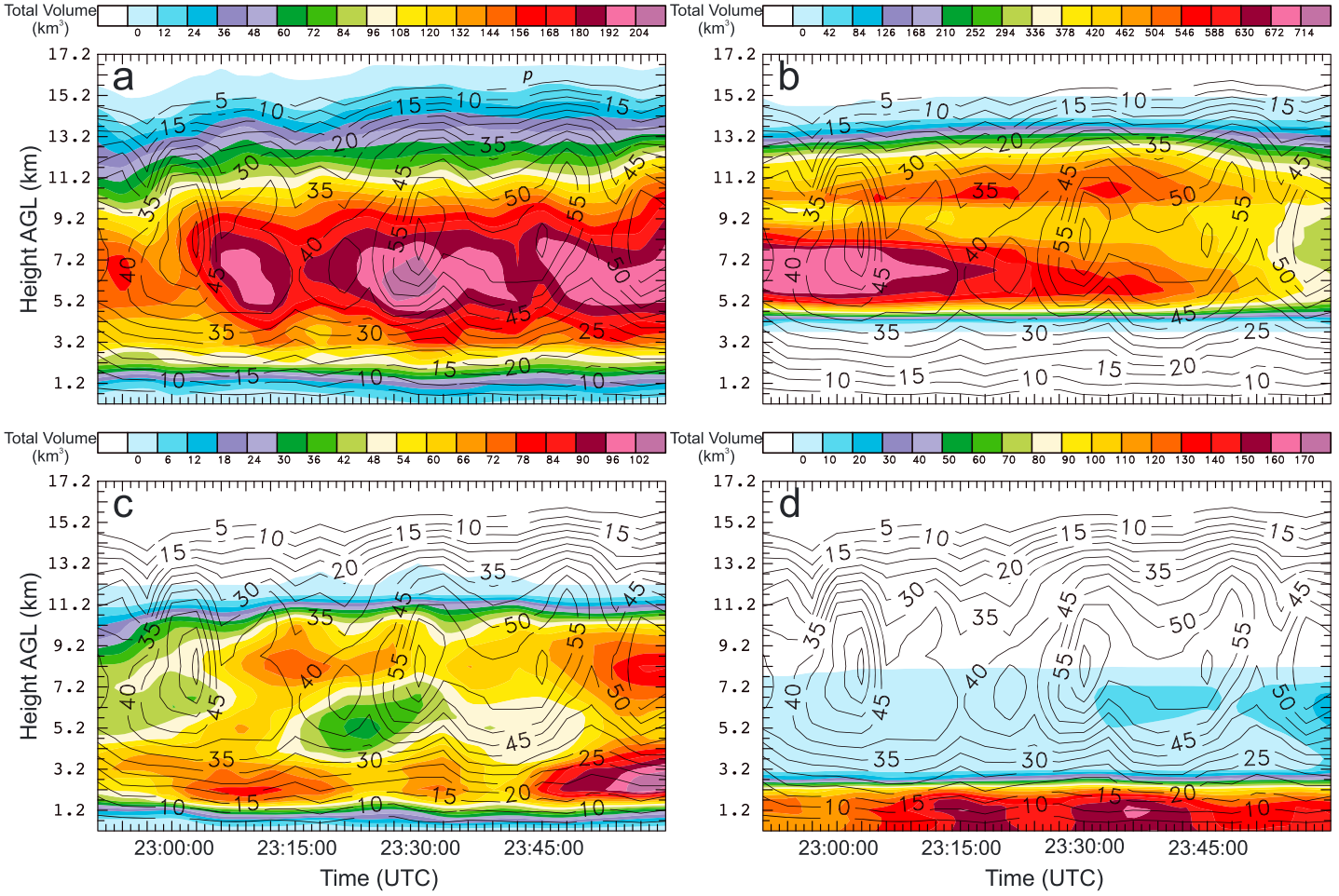

Figure 13. Time-height plots of contoured maximum updraft speed (m s^{-1}) superimposed on color-shaded DLA microphysical parameters: (a) graupel/hail volume (km^3), (b) snow volume (km^3), (c) cloud water volume (km^3), and (d) rainwater volume (km^3). Major tickmarks on the horizontal axis are at 3 min intervals indicating the time-spaced radar analysis and DLA times.

5 g kg^{-1} (Figure 12d) above the freezing level was forced by upward transport of recycled graupel/hail-meltwater raindrops within the edge of the updraft [e.g., *Ziegler*, 1988], beginning with and continuing after the second, third, and fourth updraft pulses noted above at approximately 2318, 2330, and 2348. Snow volume with peak snow mixing ratios up to 1 g kg^{-1} (Appendix A) was modulated by midlevel detrainment and upper level anvil outflow associated with the edge of the updraft and thus was rather weakly correlated to individual updraft core redevelopments (Figure 13b). Local low-level peak rain mixing ratios at around 2315, 2330, and 2351 lagged peak graupel/hail mixing ratios at around 8 km by roughly 15 min, implying a recycling process in which the low-level rain core is modulated by descent and melting of graupel/hail below the melting level either outside the updraft core or in downdraft [*Ziegler and MacGorman*, 1994].

The time-height plot of VHF source density during the dual-Doppler analysis period shows that the largest values tended to gradually elevate with time through the 8–10 km layer (Figure 14) as the storm intensified (Figure 10), as also previously noted in other supercell storms [*MacGorman et al.*, 2005, 2008; *Bruning et al.*, 2010; *Calhoun et al.*, 2013]. The timing of increases in VHF counts at this level is similar to the timing of increases of updraft mass flux (Figure 11a), updraft volume (Figure 11d), and graupel volume (Figure 13a) within the 5–9 km layer and so indicates similar pulsing behavior.

Values of VHF source density ≥10 min^{-1} per 500 m depth extended above the equilibrium level in the overshooting top during several updraft pulses. These features will be referred to as VHF overshooting top signatures (e.g., those denoted with black dashed lines in Figure 14). This signature is commonly observed in

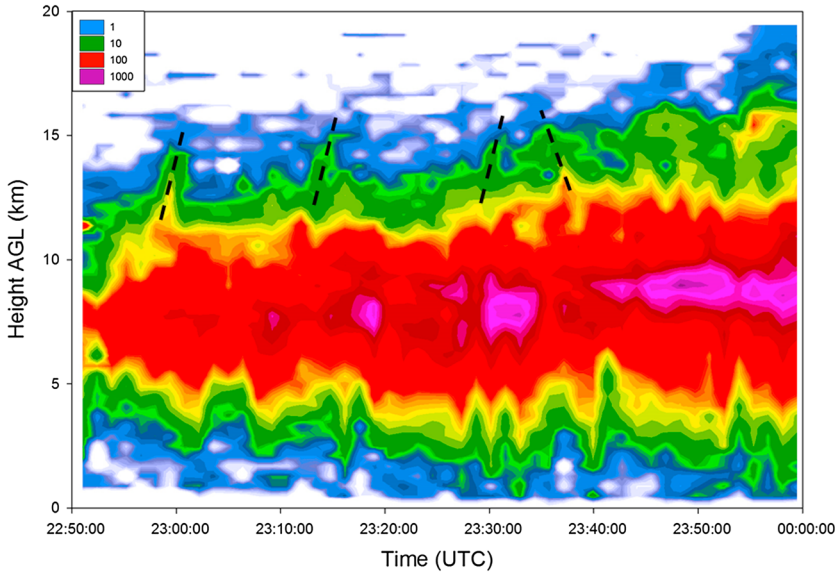

Figure 14. Time-height plot of vertical VHF source density for the multi-Doppler analysis period. The black dashed lines denote the pulsing overshooting top signatures. An overshooting top signature is maintained consistently at the end of the period, starting shortly after 2340.

supercell storms as rapidly rising updraft pulses extend above their equilibrium level [*MacGorman et al*., 2008; *Calhoun et al*., 2013; *Elliott*, 2013]. The latter studies revealed that discharges in the overshooting tops were different from those at lower altitudes, in that they consisted of continual, isolated VHF sources at low rates rather than being clustered (as occurs lower in the storm) in bursts of many VHF sources with each burst having cohesive flash structure. Some VHF overshooting top signatures appear to ascend with time (e.g., the first three indicated in Figure 14), while others appear to begin in the upper part of the overshooting top and can descend with time (e.g., the fourth signature indicated in Figure 14) as the overshooting top settles back toward the equilibrium level. The duration and maximum altitude of the VHF overshooting top signature tended to increase with time until it was maintained above the equilibrium level throughout the remainder of the period after approximately 2340, in good agreement with the DLA-derived cloud and precipitation fields, whose tops gradually rose from around 15 km to 17 km (Figures 12 and 13).

As noted previously, the storm developed an increasingly supercellular appearance as the main midlevel vertical vorticity maximum descended to the lowest analyzed altitude around 0000 (Figure 11c), indicating the presence of a deep mesocyclone [e.g., *Brandes*, 1978; *Markowski et al*., 2008]. The steady increases in total flash rates and midlevel VHF source densities and a persistent overshooting top signature after 0000 (Figures 7 and 9) are consistent with electrical characteristics of previously investigated supercell storms [e.g., *Calhoun et al*., 2013; *MacGorman et al*., 2005; *Bruning et al*., 2010; *Emersic et al*., 2011]. The number of large hail reports and the eventual development of giant hail exceeding 10 cm in diameter (Figure 8), the subsequent occurrence of a weak EF-1 tornado (located 4.827 km southwest of Piedmont at 0130), and the storm's radar reflectivity structure from KTLX (Figure 6) all further indicate that the storm maintained its supercell characteristics and continued strengthening throughout its mature phase after 0000.

5.2. Spatial Distributions of Lighting, Kinematics, and Microphysics at 2321 and 0000

An examination of radar and Lagrangian analyses at 2321 and 0000 provides a more detailed summary of the storm's initial rapid intensification period and the relationships of lightning to the changes of kinematics and microphysics during the latter period.

The vertical reflectivity structure at 2321 exhibits a weak echo vault or bounded weak echo region (BWER) [e.g., *Markowski*, 2002] on the west side of the storm (Figures 15a, 15c, and 16a) that tilts in the vertical toward the northeast. Although the BWER existed within the strong updraft region, the minimum in reflectivity was shifted toward the east of the region of strong diverging flow around the midlevel core of largest updraft speeds (Figure 15c). A reflectivity maximum was located near the top of the updraft core (Figure 16a). The

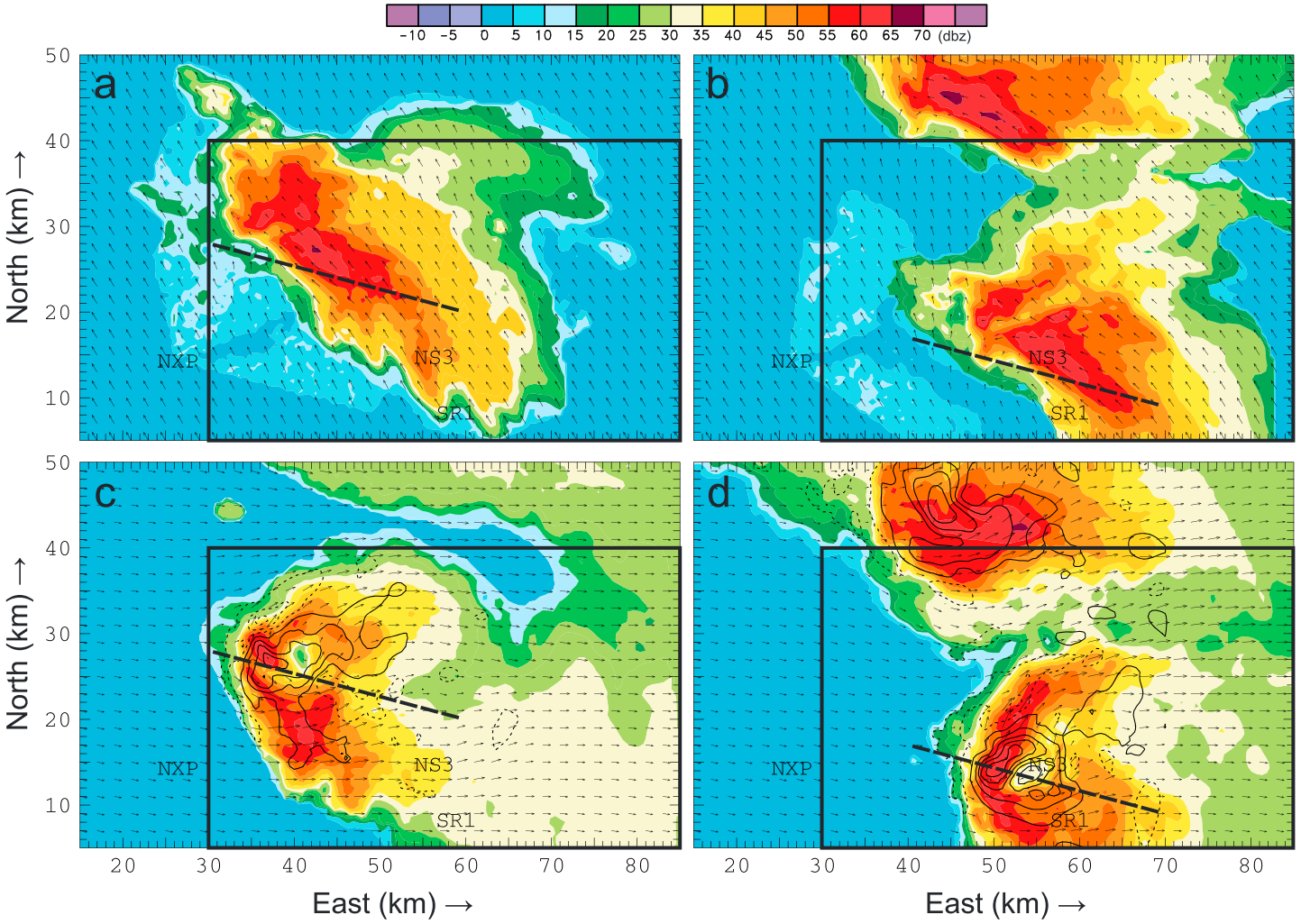

Figure 15. Radar reflectivity (dB*Z*) and dual-Doppler wind vectors at (a) 0.2 km at 2321, (b) 0.2 km at 0000, (c) 8.7 km at 2321, and (d) 8.7 km at 0000. The black dashed lines indicate the locations of the vertical cross sections shown in Figures 16 and 17, and the black boxes indicate the subarea of the domain shown in Figures 18 and 19. Vectors are scaled by 1 km = 20 m s^{-1}.

lofted reflectivity maximum was diagnosed by the DLA as graupel/hail (Figures 16a and 16b) and was maintained in the supercooled cloud core (Figure 16c) by condensation and the riming and net vertical transport of graupel/hail. The low-level meltwater rain core (Figure 16d), located in the main downdraft, was maintained by graupel/hail sedimentation and melting. The peak mixing ratios of cloud ice (Figure 16e) and snow (Figure 16f) were above and downstream from the maximum graupel/hail mixing ratio, the downstream particles having been advected to those locations by 2321, while the updraft core contained little or no ice and snow mixing ratio. The elevated graupel/hail mixing ratio core at 10.2 km was contained within and below the top of the supercooled cloud water mixing ratio core at 11.7 km, consistent with the aforementioned balance between the cloud condensation, graupel/hail riming growth, and vertical transport processes.

Although a sizable portion of the storm's anvil had moved southeastward out of the analysis domain by 0000, the updraft and the main and forward flank precipitation core remained within the domain and was more intense than at 2321 (Figures 15b and 15d versus 15a and 15c). The storm no longer contained a classic BWER structure near the updraft core. Instead, the updraft structure was more complicated than previously, with a region of strong updraft and large reflectivity having been transported downshear along the southern branch of strong diverging flow around the updraft core via a combination of horizontal advection and sedimentation (Figures 15d and 17a). A secondary plume of relatively high reflectivity was advected along the northern branch of flow around the updraft core (Figure 15d). The reflectivity minimum was collocated with

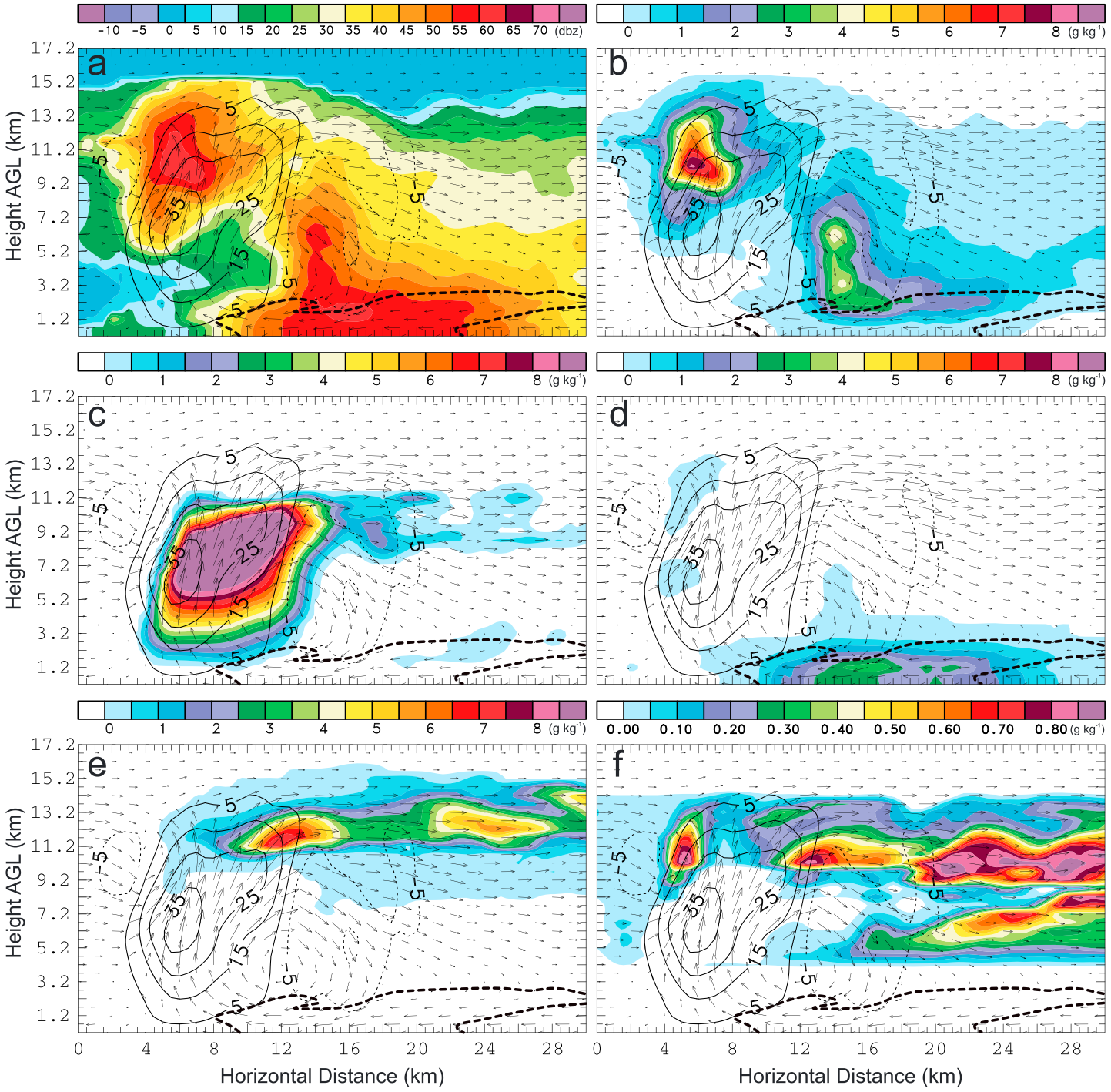

Figure 16. Vertical cross sections of vertical velocity contours (black lines) and wind vectors in this plane at 2321 UTC, superimposed on (a) mobile radar reflectivity, (b) graupel/hail mixing ratio, (c) cloud water mixing ratio, (d) rainwater mixing ratio, (e) cloud ice mixing ratio, and (f) snow mixing ratio. The heavy dashed black line indicates the −2 K contour of the perturbation θ_v field from the ambient value at each level in the 0020 mobile environmental sounding shown in Figure 5b and locates the core of the storm's cold pool. The vector length scale is 1 km = 20 m s^{-1}.

an updraft minimum in the wake of the diverging flow around the updraft at the 8.7 km level (Figure 15d). The region of large elevated reflectivity overhang in the strongest updrafts had extended downward 3–4 km (Figures 15d and 17a), likely associated with developing hail that fell to the surface a few minutes later. The reflectivity maximum collocated with the updraft was composed primarily of graupel/hail and rain (Figure 17b). Supercooled rainwater in the midlevel updraft, associated with recycled meltwater drops

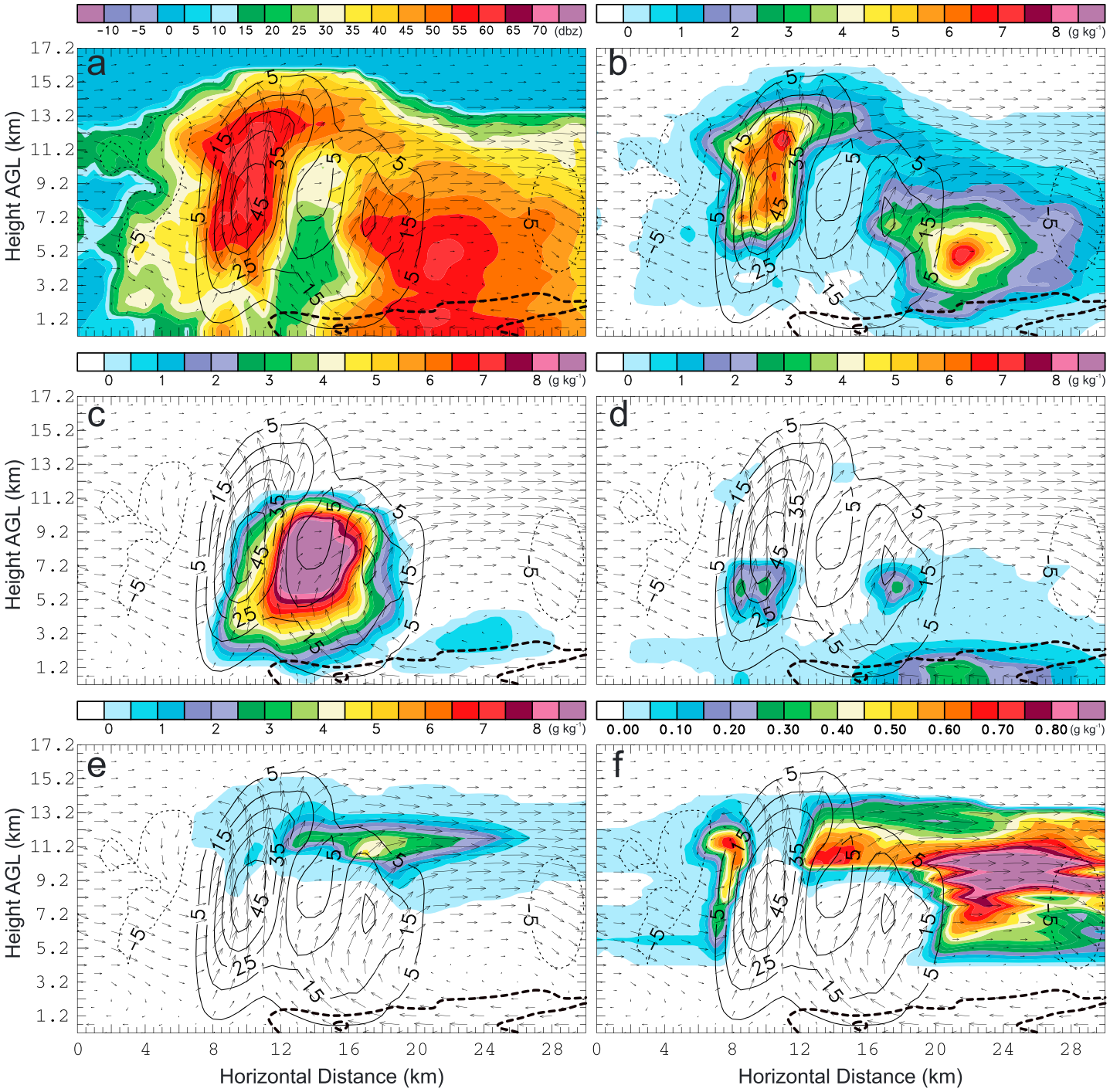

Figure 17. (a–f) Same as in Figure 16 except at 0000 UTC.

[*Ziegler*, 1988], had larger mixing ratios at 0000 than at 2321. As at 0000, the midlevel graupel/hail core continued to be collocated with the supercooled cloud core (Figure 17c) and internally consistent with cloud condensation and the riming and net vertical transport of graupel/hail, while the low-level meltwater rain core (Figure 17d) was inferred to be maintained by graupel/hail sedimentation and melting. The peak mixing ratios of cloud ice (Figure 17f) and snow (Figure 17f) were above and downstream from the maximum graupel/hail mixing ratio, the downstream particles having been advected to those locations by 0000, while the updraft core continued to contain little or no ice and snow mixing ratio. Again, substantial cloud liquid

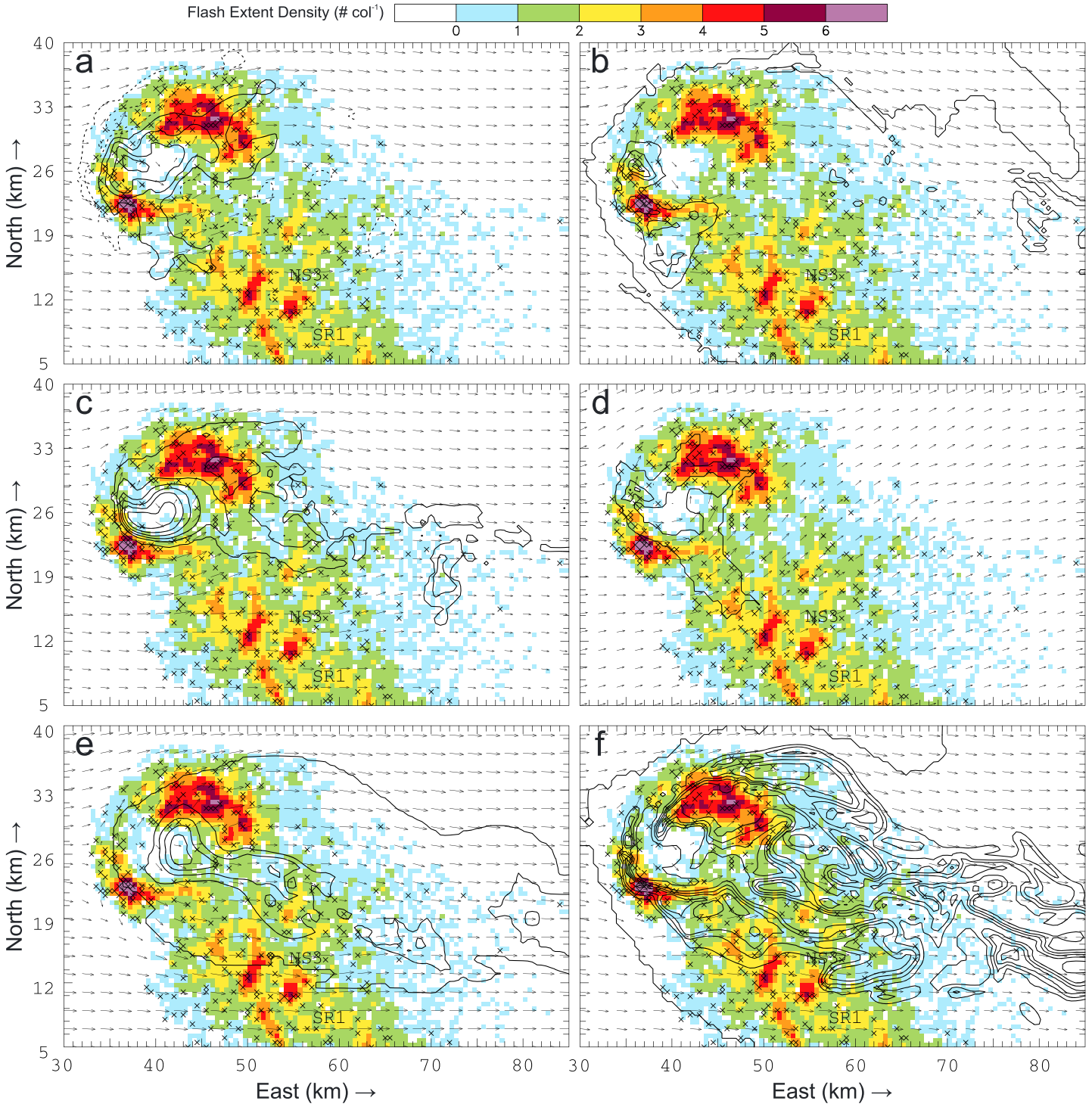

Figure 18. The color-filled flash extent density overlaid with horizontal storm-relative wind vectors and contours of updraft and hydrometeor fields at 2321 on 29 May. The contours represent the (a) updraft velocity at 8.7 km, (b) graupel/hail mixing ratio at 10.2 km, (c) cloud water mixing ratio at 8.7 km, (d) rainwater mixing ratio at 6.2 km, (e) cloud ice mixing ratio at 11.7 km, and (f) snow mixing ratio at a height of 9.7 km. Updraft contours are every 10 m s^{-1} beginning at 5 m s^{-1}. Mixing ratio contours are every 2.0 g kg^{-1} except for snow, which has contours every 0.2 g kg^{-1}. Locations of NS3 (location of first in situ balloon launch) and SR1 are indicated. The vector length scale is 1 km = 20 m s^{-1}.

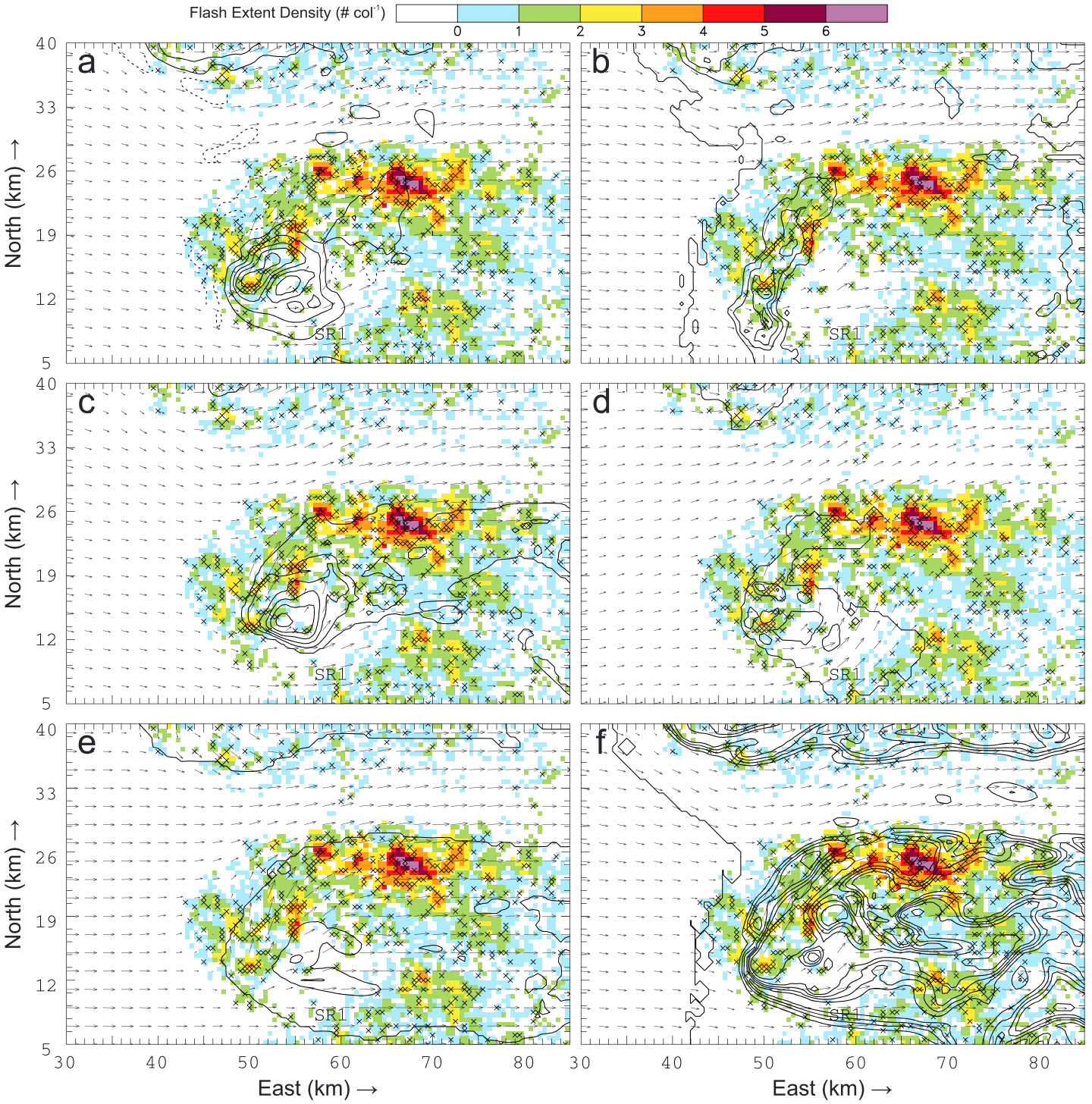

Figure 19. (a–f) Same as in Figure 18 except at 0000 UTC. NS3 was in the process of redeploying to a new location and is not indicated.

extended well above the freezing level in the main updraft and thus was consistent with electrification via noninductive charging due to ice-ice interactions among actively riming graupel. A plume of cloud liquid extended downstream at upper levels along with maxima in cloud ice and snow mixing ratios above and east of the top the larger cloud liquid mixing ratios (Figures 18 and 19), with anvil cloud liquid maxima being heavily depleted by ice particle deposition growth via the Bergeron mechanism [*Ziegler*, 1985; *Rutledge and Hobbs*, 1983].

The core of the surface-based cold outflow pool is centered within the low-level rain and graupel/hail core to the east of the main updraft at 2321 (Figure 16) and 0000 (Figure 17). The cold pool is maintained by the combined diabatic cooling from graupel/hail melting and rain evaporation [e.g., *Ziegler*, 2013b]. Although the southwestern edge of the surface-based cold pool had deepened and outflow wind speeds had increased by 0000, the cold pool remained in phase with the low-level updraft and thus contributed to the low-level convergence that helped maintain the main updraft throughout this period. The vertical cross sections of the wind field revealed convective rolls and eddies in the lowest 5–6 km. The maintained relative positions of the Kingfisher storm's updraft and cold pool are consistent with commonly accepted conceptual models of supercells [e.g., *Lemon and Doswell*, 1979], which involve cold air from downdrafts being drawn back up into the updraft to contribute to low-level baroclinic vorticity generation. Both the vorticity and the position of the outflow relative to the updraft contributed to the storm's quasi-steady state, thus allowing it to persist.

The horizontal distributions of lightning flash extent density (FED) and flash initiations within the dual-Doppler analysis domain of the Kingfisher storm are examined in the context of hydrometeor mixing ratios and updraft speeds (Figures 18 and 19) at levels near local maxima of the respective quantities within the broader 5–12 km layer that contained the largest VHF source densities (Figures 9 and 14). VHF sources were concentrated on the northeast and southwest sides of a bounded weak lightning region (BWLR; also known as a "lightning hole") at 2321 (Figure 18), the latter term being defined as a region containing a prominent bounded relative minimum in flash density [*Ziegler et al*., 2014] or VHF source density and thus also an FED minimum (i.e., similar to features noted in LMA observations of supercell storms by *Krehbiel et al*. [2000], *MacGorman et al*. [2005], *Payne et al*. [2010], and *Calhoun et al*. [2013]). The regions with FED maxima contained the denser clusters of flash initiations, but initiations were also present throughout the storm's horizontal extent. Although most of the area of strongest updraft speeds had the minimal FED of the BWLR, the surrounding ring of large FED overlapped the southwest edge of the updraft core, where the gradients in updraft speeds were large (Figure 18a). Note that the BWLR was better collocated with the BWER than either feature was with the maximum updraft [*DiGangi*, 2014, Figures 15c and 18a].

The region of large FED at 2321 on the storm's southwest flank overlapped a relative maximum of graupel/hail mixing ratio (Figure 18b), while the largest supercooled rain mixing ratios were restricted to the layer between zero and −15°C centered at 6.7 km on the western updraft flank (Figure 18d). The largest cloud ice and snow mixing ratios overlapped the large FED on both the north and south flanks of the BWLR and updraft core but extended downshear into the forward anvil, where FED values were small. The regions of largest inferred cloud water mixing ratios were collocated with the BWLR and the BWER (Figure 18c), although some liquid cloud extended into the region of large FED on the northeast side of the BWLR, where it overlapped regions of cloud ice and snow. Lightning in the southern flank of the forward anvil extended into small snow and graupel/hail mixing ratios exceeding 0.05 g kg^{-1} and 0.25 g kg^{-1}, respectively. Since the lightning densities are vertically integrated values for the column instead of lightning at a particular level, it is speculated that some mixture of in situ charging and charge transport may contribute to local electrification via a combination of microscopic and macroscopic charging involving various ice particle habits through the deeper VHF-source-bearing layer.

The largest FEDs at 0000 had migrated to the north side of the updraft core and extended several kilometers farther downshear east of the core, probably reflecting the increasing wind speeds and advection in the northern branch of horizontal flow around the updraft (Figures 15d and 19a). The larger values of FED near the west and north sides of the updraft (again a region of large updraft gradients) penetrated into the region of largest updraft speeds, rather than staying along the periphery of the updraft core as at 2321. The southern boundary of the BWLR was more tenuous at 0000 than at 2321. The FEDs bounding the lightning minimum on the east were more than 5 km from the lowest positive updraft contour, and the minimum encompassed a downdraft as well as weak updrafts. Thus, much as the reflectivity minimum would not be considered a "classic" BWER at 0000, neither would the lightning minimum at 0000 would not be considered a classic BWLR feature. Flash initiations tended to cluster near the FED maximum on the northern flank of the storm and in or near the strong gradient in updraft speed on the western flank of the updraft core.

Although the storm evolved considerably between 2321 and 0000, the spatial relationships of FEDs with the mixing ratios diagnosed by the DLA nevertheless remained similar (Figure 18 versus 19). Inferred cloud water mixing ratios, for example, were greatest in a region with little or no lightning, although some flashes did

enter the western and northern flanks of the cloud liquid region (Figure 19c). Cloud ice extended over much of the Kingfisher storm but maximized in regions of updraft, part of which contained FED maxima (Figures 19a and 19e). Graupel/hail and snow extended over almost the whole region of the Kingfisher storm (Figures 19b and 19f). The largest supercooled rain mixing ratios were again restricted to the layer between zero and −15°C centered at 6.7 km with a relative maximum on the western updraft flank and lesser amounts in the weaker ring-shaped updraft core extending to the east (Figure 19d). However, the relative lightning maxima on the western and northern flanks of the updraft core overlapped maxima in graupel/hail mixing ratios, while the FED minimum in regions of weak vertical motions east of the updraft core also had a minimum in graupel/hail mixing ratio (Figures 19a and 19b). The largest FED values on the northern and northeastern flanks of the updraft core were near and within snow mixing ratio maxima, and the region of little or no lightning to the east of the updraft core overlapped an extensive relative minimum in snow mixing ratios (Figures 19a and 19f).

6. Discussion and Conclusions

The 29 May 2012 case presented here is one of the five principal cases selected by DC3 scientists for intensive study and is the only supercell case selected [*Barth et al*., 2015]. The storm analyzed in this paper was the southernmost supercell in a broken line of severe storms, and it intensified during the period observed by DC3 scientists, with flash rates increasing from 5–15 min^{-1} to approximately 120 min^{-1} and vertical vorticity increasing to $34 \times 10^{-3}\,s^{-1}$ during the period observed by DC3. After DC3 mobile radar, sounding, and aircraft observations ended, the storm continued to intensify and eventually produced hail up to approximately 12 cm (5 inch) in diameter, flash rates exceeding 400 min^{-1}, and a weak EF-1 tornado.

The data presented in this paper were obtained by three mobile radars, the OK-LMA, and the mobile environmental soundings. The three aircraft participating in DC3 made extensive measurements of chemical species, aerosols, cloud condensation nucleus, radiation, and standard meteorological parameters in the BL inflow and anvil outflow of the severe storm complex. Several studies by other investigators are using these data and storm simulations to investigate the transport and production of chemical species by the storm [e.g., *Yang et al*., 2015], including the production of NO_x by lightning. Besides providing an opportunity to study how lightning production affects various storm properties and vice versa, the present study provides the atmospheric soundings, wind fields, lightning observations, and estimates of microphysics needed to help evaluate the model simulations of microphysics and chemical transport and production by the storm. Data from the balloon-borne electric field meter and NSSL videosonde particle imager [*Waugh et al*., 2015] are the subject of another study focusing on the in situ microphysics and its relationship to measured radar parameters and electric fields in this and other DC3 storms.

The microphysical properties inferred by the DLA from the reflectivity and wind fields obtained from the mobile radars for this case and described in the previous section of this paper are similar to what was reported by *Heymsfield and Musil* [1982] from flights through a Colorado hailstorm. In situ measurements obtained during their instrumented T-28 storm penetration aircraft's first traverse of the storm core revealed several important storm features that were similar to the retrieved DLA fields at 2321 (Figures 16 and 17): (1) a cyclonically curved band of ice particles and graupel along the southern updraft flank that provided a source of ice particles to grow within the updraft; (2) a relative minimum of ice particle size and concentration within the updraft core that also contained large supercooled liquid cloud contents; (3) high concentrations of small and moderately sized ice particles, especially graupel and rimed aggregates, on the west side of the updraft; and (4) a mix of rimed and unrimed particles on the east side of the updraft and in downshear downdrafts. *Heymsfield and Musil* [1982] also reported detections of graupel within the updraft during the second T-28 penetration, as also obtained by the DLA in the Kingfisher storm at 0000 (Figures 17 and 19).

The microphysical quantities retrieved by the DLA (Figures 18 and 19) are broadly consistent with charge separation via the noninductive mechanism, which is thought to be the dominant mechanism by which thunderstorms become electrified [e.g., *MacGorman and Rust*, 1998, sections 3.5.3 and 7.18; *Ziegler and MacGorman*, 1994; *Wiens et al*., 2005]. This mechanism involves rebounding collisions between actively riming graupel and smaller ice particles and is typically greatest in the mixed-phase region of a storm's updraft [e.g., *Takahashi and Miyawaki*, 2002; *Emersic and Saunders*, 2010]. The necessary supercooled cloud water extended well above the 0°C isotherm in the updraft (i.e., from approximately 5 km agl to 11 km

in the moist-adiabatic updraft sounding) and overlapped regions of graupel, cloud ice, and snow (Figures 16–19). Furthermore, the timing of increases in VHF counts in the 8–10 km layer in the time-height plots, which contained the largest VHF source counts (Figures 9 and 14), is similar to the timing of increases in updraft mass flux (Figure 11b), updraft volume (Figure 11d), and graupel volume (Figure 11a) at approximately 5–9 km agl. Although some increases in VHF source counts associated with little or no increase in one or more of the other storm parameters, at least one of the other parameters had an increase near the time of every VHF increase, a pattern which indicates a similar dependence on updraft pulses, as one would expect from the noninductive graupel-ice mechanism since kinematic intensification would be expected to increase both concentrations and sizes of small deposition-grown ice particles and larger rimed ice particles, which in turn would accelerate the in situ charging rates.

Lightning FEDs tended to overlap regions of graupel, cloud ice, and snow in the 6–12 km layer, while also extending into portions of the downstream anvil that contained graupel with rather small snow and ice mixing ratios (Figures 18 and 19). It should be noted that significant ice concentrations are likely present even if mixing ratio values are small, thus maintaining support for charge transport and possibly also in situ charging. The eastern, downstream portions of both vertical and horizontal cross sections show elevated maxima in cloud ice and snow mixing ratios, which were likely advected there, along with any charge they carried, away from the updraft region following an earlier updraft pulse. These relationships with the FEDs can be interpreted as consistent with the locations at which one might expect charge carriers from the noninductive graupel-ice electrification mechanism to be.

The charge distribution at any time is the result of electrification processes and particle advection that occurred during previous times. Thus, a four-dimensional analysis of the distribution of lightning and microphysical species is required to provide firm support for electrification mechanisms from observations, and obtaining the observational data sets needed to perform such an analysis is difficult. However, storm simulations that simultaneously track microphysics, electrification processes, and lightning have found that rebounding collisions between graupel and cloud ice particles would produce distributions of lightning relative to other storm properties similar to those reported here [e.g., *Mansell et al*., 2002; *Kuhlman et al*., 2006; *Fierro et al*., 2006; *Calhoun et al*., 2014].

The evolution of the BWLRs in the Kingfisher storm evince some similarities but also differences relative to the classical conceptual model based on previous analyses of lightning holes or lightning rings. As in the present case at 2321 (Figure 18), the BWLRs in previous studies were also coincident with weaker reflectivities in the region of strongest updrafts [e.g., *Krehbiel et al*., 2000; *MacGorman et al*., 2005, 2008; *Wiens et al*., 2005; *Kuhlman et al*., 2006; *Payne et al*., 2010; *Calhoun et al*., 2013]. Additionally, the BWER and BWLR in both the present and earlier studies were hypothesized to have formed via the elevation of graupel/hail which had developed in the updraft, with the BWLR forming both somewhat higher and later than the BWER owing to the time for macroscopic separation and transport of opposite charge polarities following the in situ microscopic graupel/hail-ice charging. The lightning and reflectivities in the present and previous cases that bound the BWLR and BWER, respectively, are hypothesized to originate from the cascade of precipitating charged graupel/hail surrounding the updraft core [e.g., *Payne et al*., 2010]. According to the classical BWLR dissipation model, lightning eventually extends into the region of strongest updrafts and infills the former BWLR as the updraft weakens and the former BWER fills with charging graupel/hail associated with the occlusion of the cycling mesocyclonic updraft.

The coevolutions of kinematic, microphysical, and lightning fields in the Kingfisher storm also bore some differences in comparison to the aforementioned earlier studies. For example, the BWLR at 8.7 km mean sea level was located to the east of the updraft core, spanned a broad region of weaker updrafts, and incorporated a small downdraft by 0000 (Figure 19). Another difference was that the cold surface outflow remained to the east of the inflow and had not undercut the updraft to weaken it as the BWLR weakened at 0000 (Figure 17). The updraft actually intensified as reflectivity and lightning began filling much of the updraft core (compare Figures 18 and 19); the region of elevated large reflectivities had grown several kilometers downward inside the updraft core (compare Figures 16 and 17), a characteristic toward the heavy-precipitation end of the supercell spectrum. The largest FEDs bounding the BWLR were along the strong northern branch of flow around the updraft, and this boundary extended far downshear of the updraft core and mesocyclone. Lightning densities bounding the BWLR on the south and east were smaller than

those along the north side and were in the weaker southern branch of flow around the updraft, again extending far downshear from the updraft core and mesocyclone. It appears that the BWLR at 0000 was due to a wake in the flow and advection of charged hydrometeors around the updraft, rather than being due to a precipitation cascade around the updraft core and mesocyclone.

Appendix A: Addition of Cloud Ice and Snow Fields to the DLA

The diagnosis of snow mixing ratio (q_s) and the prediction of cloud ice mixing ratio (q_x) by the DLA follow general methods described by Z13 and *Ziegler* [2013b]. These additional fields are useful because cloud ice and snow particles are important carriers of noninductively separated charges associated with rebounding collisions between graupel/hail and either cloud ice or snow particles in mixed-phase storm updrafts [*MacGorman and Rust*, 1998].

A1. Diagnosis of Snow Mixing Ratio

The diagnosis of q_s (g kg^{-1}) is based on the physical principle that ice supersaturation is generated within deep volumes of weak to moderate subfreezing updrafts that enhance subsequent in situ snow crystal nucleation and deposition growth [e.g., *Pruppacher and Klett*, 1978]. Examination of backward grid point air trajectories that span the subfreezing region of a simulated supercell [*Ziegler et al.*, 2010; Z13] reveals a significant correspondence between q_s values at the DLA grid points and the maximum updraft strength w_{max} (m s^{-1}) encountered during the subfreezing portion of the backward trajectories. The grid point q_s values also tend to maximize at the midanvil level and approach zero at the melting level and anvil top. The simulation data also indicate that grid point q_s values trend toward zero as w_{max} values either approach zero or exceed a height-dependent threshold updraft strength.

The height-dependent maximum snow mixing ratio q_{s0} (g kg^{-1}) in the storm is accordingly parameterized by the expression

$$q_{s0}(z^*) = Q_{max} \sin[\pi(z^* - H_{melt})/(H_{anvil} - H_{melt})], \quad \text{(A1)}$$

where Q_{max} (g kg^{-1}) is the assumed global maximum snow mixing ratio in the storm, H_{melt} is the melting level height (km), z^* (km) $= z + (3.9 - H_{melt})$ is the morphed height relative to the actual height z [Z13], and H_{anvil} is the height (km) at the top of the snow-bearing anvil layer (Table A1). The diagnosed q_s (g kg^{-1}) value is parameterized via the Gaussian functional form

$$q_s = q_{s0}(z^*) \exp\left\{-[w_{max} - W_{max0}(z^*)]^2 / \left[2S_{qs}(z^*)^2\right]\right\}, \quad \text{(A2)}$$

where $W_{max\,0}$ (m s^{-1}) and S_{qs} (m s^{-1}) are the height-dependent coefficients (Table A2). Although the basic functional forms of equations (A1) and (A2) are inferred from the earlier simulated Binger supercell (which contained a Q_{max} of only ~0.2 g kg^{-1}), a more physically realistic value of $Q_{max} = 1$ g kg^{-1} [e.g., *Heymsfield*

Table A1. List of New and Altered Parameters Contained in Diagnostic Relationships for Precipitation Quantities in the DLA as Applied to the 29 May 2012 Kingfisher Storm[a]

Parameter (Units)	Symbol	Value
Storm-maximum snow mixing ratio (g kg^{-1})	Q_{max}	1.0
Environmental melting level height (km agl)	H_{melt}	4.0
Height (km agl) of −15°C in updraft core	H_{frz}	7.7
Height (km agl) of snow-containing anvil top	H_{anvil}	14.5
Snow intercept parameter (m^{-4})	n_{0s}	8×10^6
Snow density (kg m^{-3})	ρ_s	100
Z_{es} coefficient in equation (A4)	C_s	7.295×10^{19}
Bigg freezing coefficient in equation (A7)	α_{frz}	1.5
Wet-hail threshold reflectivity (dBZ)	Z_{hail}	60.0
Δq_g per dBZ (g kg^{-1} dBZ^{-1}) for $Z > Z_{hail}$	Δq_g	0.1
Cloud-freezing coefficient in equation (A10)	C_{frzc}	1.0
Cloud-freezing onset temperature (K) in equation (A10)	T_{frzc}	233.15

[a]The symbol and values of the various parameters are also listed. Other unlisted DLA parameters are as described in *Ziegler* [2013a, 2013b].

Table A2. Look-Up Table Values of $W_{max\,0}(z^*)$ and $S_{qs}(z^*)$ Parameters Contained in Diagnostic Equation (A2) for Snow Mixing Ratio in the Updated DLA as Applied to the 29 May 2012 Kingfisher Storm[a]

Height (km agl)	W_{max0} (m s^{-1})	S_{qs} (m s^{-1})
5.0	6.0	3.0
6.0	7.0	3.0
7.0	8.0	3.0
8.0	12.0	4.0
9.0	15.0	5.0
10.0	20.0	8.0

[a]Since equation (A2) is itself a function of height, the value within each 0.5 km layer is held constant at the specified value of the layer's lower level. Values below 4 km and above 10 km take the 4 km and 10 km values, respectively.

and Musil, 1982] is inferred from recent supercell storm simulations with improved multimoment microphysical parameterizations [*Ziegler et al.*, 2014] (E. Mansell, personal communication, 2015).

The snow size distribution follows supporting information in *Gilmore et al.* [2004] (hereafter G04) and takes the inverse exponential form

$$n_s(D) = n_{0s}\exp(-\lambda_s D), \tag{A3}$$

where n_{0s} (m^{-4}) is the intercept parameter, $\lambda_s = 1/\overline{D_{ns}}$ (m^{-1}) is the slope parameter, and $\overline{D_{ns}}$ is the concentration-weighted mean diameter. The total snow concentration N_s (m^{-3}) and q_s are related to other distribution parameters via equations (5) and (6) in Z13 with subscript $x = s$. The equivalent snow radar reflectivity factor Z_{es} (mm^6 m^{-3}) takes the same form as equation (8) in Z13 with substitution of subscripts (i.e., $g \rightarrow s$) and the assumption that $C_s = C_g$. Substituting the expression for q_s yields the alternate reflectivity factor expression

$$Z_{es} = \alpha_r C_s \pi \rho_a \rho_s q_s / \left(\rho_w{}^2 \lambda_s{}^3\right), \tag{A4}$$

where ρ_a is the air density (kg m^{-3}); ρ_s and ρ_w are the densities of snow and water (kg m^{-3}), respectively; and other terms are defined in Z13. If Z_{es} locally exceeds the measured total equivalent reflectivity factor Z_{eh}, a revised thresholded q_s (g kg^{-1}) value is calculated as

$$q_s = \left\{\left[Z_{eh}\rho_w{}^2\left(10^{-3}\rho_a/\pi\rho_s n_{0s}\right)^{-(3/4)}\right]/\left(10^{-3}\alpha_r C_s \pi \rho_a \rho_s\right)\right\}^{4/7}, \tag{A5}$$

followed by recalculation of the snow distribution parameters.

Extending the approach of Z13, closure is imposed on the updated mixed-phase precipitation field by partitioning the measured total equivalent reflectivity factor assuming that $Z_{eh} = Z_{er} + Z_{eg} + Z_{es}$. Following calculation of snow quantities, a residual total equivalent reflectivity factor

$$(Z_{eh})_{res} = Z_{eh} - Z_{es} \tag{A6}$$

is now used in place of Z_{eh} to calculate graupel/hail and rain quantities following the general method described by Z13. Typical snow reflectivities using the above treatment are up to ~25–30 dBZ, with minimal impact on small graupel/hail mixing ratio (q_g) values in the anvil and essentially no effect on q_g in the high-reflectivity storm core.

The heterogeneous rain-freezing adjustment has been updated to produce a more physically consistent transition from supercooled rain to graupel/hail reflectivity and mixing ratio with increasing altitude in subfreezing updrafts of variable intensity. Equations (15) and (16) of Z13 are replaced by the single expression

$$q_g = \left\langle (1 - w^*) + w^* \exp\left\{-\left[\alpha_{frz}(H_{frz} - z^*)/(H_{frz} - H_{melt})\right]^2\right\}\right\rangle q_g{}^*, \tag{A7}$$

where w^* and $q_g{}^*$ are the updraft scale and provisional graupel/hail mixing ratio [Z13]. The ratio $q_g/q_g{}^*$ decreases from unity at H_{frz} (i.e., complete rain freezing) to ~0.1 at H_{melt} for $\alpha_{frz} = 1.5$ (Table A1) and $w \geq w_{max}$.

A simple correction has also been added to account for effects of reflectivity exceeding a specified "wet hail threshold." The condition Z_H (dBZ) $> Z_{hail}$ is assumed to indicate surface wetting of hail in a state of either melting ($z^* < H_{melt}$) or wet growth ($z^* > H_{melt}$). An expanded, thresholded version of equation (11) in Z13 for the case of $Z_H > Z_{hail}$ takes the form

$$\left(Q_g\right)^* = \varepsilon_g \exp\left\{\left[Z_{hail} - Z_{0g}(z^*)\right]/\left[S_0(z^*)\right]_{q_g}\right\} \tag{A8}$$

and

$$q_g = \left(Q_g\right)^* + \left[\Delta q_g (Z_H - Z_{hail})\right], \tag{A9}$$

where $(Q_g)^*$ is the thresholded graupel/hail mixing ratio (g kg^{-1}) and Δq_g is the rate of change of q_g with reflectivity (dBZ) in excess of Z_{hail} (dBZ). A value of $Z_{\text{hail}} = 60$ dBZ is appropriate to denote the onset of large, wet hail [*Straka et al.*, 2000]. Parameter values for the 29 May 2012 storm study are listed in Table A1.

A2. Prediction of Cloud Ice Mixing Ratio

The Lagrangian prediction of q_x (g kg^{-1}) follows the same general methods as the prediction of cloud water [Z13]. The cloud ice microphysical processes include vapor nucleation [G04], vapor deposition [*Rutledge and Hobbs*, 1983], sublimation [*Ziegler*, 1985], collection by rain and graupel/hail [G04], and cloud water freezing (equation (A10)). The Lagrangian cloud water freezing rate is parameterized according to the expression

$$(dq_c/dt)_{\text{frzc}} = q_c\{1 - \exp[-C_{\text{frzc}}(T_{\text{frzc}} - T_K)]\}/\Delta t, \tag{A10}$$

where T_K is the temperature (K), T_{frzc} is the onset temperature of cloud freezing (K), $T_K < T_{\text{frzc}}$, and $\Delta t = 20$ s is the Lagrangian time step. Coefficient values for equation (A10) in the 29 May 2012 storm study are listed in Table A1.

Acknowledgments
The authors thank Alan Shapiro and Susan Postawko for their useful discussions that helped improve the manuscript. The authors also gratefully acknowledge Matthew Elliot, Eric Bruning, and Ron Thomas, who assisted with lightning analysis procedures; Ben Herzog and Kristin Calhoun, who assisted with WDSS-II applications; Doug Kennedy and Dennis Nealson for maintaining the OKLMA; and James Russell and Steve Fletcher, who provided assistance with coding and computer support. This research was sponsored by NSF grants AGS-1063945 and AGS-1063537 and by a NASA Earth and Space Sciences Fellowship. Data used in this study are listed in the references.

References

Barth, M. C., et al. (2015), The Deep Convective Clouds and Chemistry (DC3) field campaign, *Bull. Am. Meteorol. Soc.*, *96*(8), 1281–1310, doi:10.1175/BAMS-D-13-00290.1.

Barth, M. C., et al. (2016), Convective transport and scavenging of peroxides by thunderstorms observed over the Central U.S. during DC3, *J. Geophys. Res. Atmos.*, *121*, 4272–4295, doi:10.1002/2015JD024570.

Biggerstaff, M. (2014a), Mobile SMART Radar-1 Data, version 1.0, UCAR/NCAR - Earth Obs. Lab. [Available at http://data.eol.ucar.edu/dataset/353.216, Accessed 02 Oct 2013.]

Biggerstaff, M. (2014b), Mobile SMART Radar-2 Data, version 1.0, UCAR/NCAR - Earth Obs. Lab. [Available at http://data.eol.ucar.edu/dataset/353.217, Accessed 02 Oct 2013.]

Biggerstaff, M. I., L. J. Wicker, J. Guynes, C. Ziegler, J. M. Straka, E. N. Rasmussen, A. Doggett, L. D. Carey, J. L. Schroeder, and C. Weiss (2005), The shared mobile atmospheric research and teaching radar: A collaboration to enhance research and teaching, *Bull. Am. Meteorol. Soc.*, *86*(9), 1263–1274, doi:10.1175/BAMS-86-9-1263.

Brandes, E. A. (1978), Mesocyclone evolution and tornadogenesis: Some observations, *Mon. Weather Rev.*, *106*(7), 995–1011, doi:10.1175/1520-0493(1978)106<0995:MEATSO>2.0.CO;2.

Brandes, E. A. (1984), Relationships between radar-derived thermodynamic variables and tornadogenesis, *Mon. Weather Rev.*, *112*(5), 1033–1052, doi:10.1175/1520-0493(1984)112<1033:RBRDTV>2.0.CO;2.

Bruning, E. C., W. D. Rust, D. R. MacGorman, M. I. Biggerstaff, and T. J. Schuur (2010), Formation of charge structures in a supercell, *Mon. Weather Rev.*, *138*(10), 3740–3761, doi:10.1175/2010MWR3160.1.

Bunkers, M. J., M. R. Hjelmfelt, and P. L. Smith (2006), An observational examination of long-lived supercells. Part I: Characteristics, evolution, and demise, *Weather Forecasting*, *21*(5), 673–688, doi:10.1175/WAF949.1.

Burgess, D. W., E. R. Mansell, C. M. Schwarz, and B. J. Allen (2010), Tornado and tornadogenesis events seen by the NOXP, X-band, dual-polarization radar during VORTEX2 2010, paper 5.2 presented at 25th Conference on Severe Local Storms, Am. Meteorol. Soc., Denver, Colo. [Available at https://ams.confex.com/ams/25SLS/techprogram/paper_176164.htm.]

Calhoun, K. M., D. R. MacGorman, C. L. Ziegler, and M. I. Biggerstaff (2013), Evolution of lightning activity and storm charge relative to dual-Doppler analysis of a high-precipitation supercell storm, *Mon. Weather Rev.*, *141*(7), 2199–2223, doi:10.1175/MWR-D-12-00258.1.

Calhoun, K. M., E. R. Mansell, D. R. MacGorman, and D. C. Dowell (2014), Numerical simulations of lightning and storm charge of the 29–30 May 2004 Geary, Oklahoma, supercell thunderstorm using EnKF Mobile Radar Data Assimilation, *Mon. Weather Rev.*, *142*(11), 3977–3997, doi:10.1175/MWR-D-13-00403.1.

Carey, L., and S. Rutledge (1996), A multiparameter radar case study of the microphysical and kinematic evolution of a lightning producing storm, *Meteorol. Atmos. Phys.*, *59*(1–2), 33–64.

Crum, T. D., and R. L. Alberty (1993), The WSR-88D and the WSR-88D Operational Support Facility, *Bull. Am. Meteorol. Soc.*, *74*(9), 1669–1687, doi:10.1175/1520-0477(1993)074<1669:TWATWO>2.0.CO;2.

Cummins, K. L., and M. J. Murphy (2009), An overview of lightning locating systems: History, techniques, and data uses, with an in-depth look at the U.S. NLDN, *IEEE Trans. Electromagn. Compat.*, *51*(3), 499–518, doi:10.1109/TEMC.2009.2023450.

Deierling, W., and W. A. Petersen (2008), Total lightning activity as an indicator of updraft characteristics, *J. Geophys. Res.*, *113*, D16210, doi:10.1029/2007JD009598.

DiGangi, E. (2014), A study of the electrical, kinematic, and microphysical properties of the 29 May 2012 Kingfisher supercell, MS thesis, 106 pp., Sch. of Meteorol., The Univ. of Oklahoma. [Available at http://hdl.handle.net/11244/14246.]

Elliott, M. S. (2013), Electrical discharges in the overshooting tops of thunderstorms, MS thesis, 139 pp., Sch. of Meteorol., Univ. of Oklahoma.

Emersic, C., and C. P. R. Saunders (2010), Further laboratory investigations into the relative diffusional growth rate theory of thunderstorm electrification, *Atmos. Res.*, *98*(2–4), 327–340, doi:10.1016/j.atmosres.2010.07.011.

Emersic, C., P. L. Heinselman, D. R. MacGorman, and E. C. Bruning (2011), Lightning activity in a hail-producing storm observed with phased-array radar, *Mon. Weather Rev.*, *139*(6), 1809–1825, doi:10.1175/2010MWR3574.1.

Fierro, A. O., M. S. Gilmore, E. R. Mansell, L. J. Wicker, and J. M. Straka (2006), Electrification and lightning in an idealized boundary-crossing supercell simulation of 2 June 1995, *Mon. Weather Rev.*, *134*(11), 3149–3172, doi:10.1175/MWR3231.1.

Gilmore, M. S., J. M. Straka, and E. N. Rasmussen (2004), Precipitation and evolution sensitivity in simulated deep convective storms: Comparisons between liquid-only and simple ice and liquid phase microphysics, *Mon. Weather Rev.*, *132*(8), 1897–1916, doi:10.1175/1520-0493(2004)132<1897:PAESIS>2.0.CO;2.

Herzog, B. (2013), Total lightning information in a 5-year thunderstorm climatology, MS thesis, 114 pp., Sch. of Meteorol., The Univ. of Oklahoma.

Heymsfield, A. J., and D. J. Musil (1982), Case study of a hailstorm in Colorado. Part II: Particle growth processes at mid-levels deduced from in-situ measurements, *J. Atmos. Sci.*, *39*(12), 2847–2866, doi:10.1175/1520-0469(1982)039<2847:CSOAHI>2.0.CO;2.

Heymsfield, A. J., A. R. Jameson, and H. W. Frank (1980), Hail growth mechanisms in a Colorado storm: Part II: Hail formation processes, *J. Atmos. Sci.*, *37*(8), 1779–1807, doi:10.1175/1520-0469(1980)037<1779:HGMIAC>2.0.CO;2.

Kain, J. S., et al. (2013), A feasibility study for probabilistic convection initiation forecasts based on explicit numerical guidance, *Bull. Am. Meteorol. Soc.*, *94*(8), 1213–1225, doi:10.1175/BAMS-D-11-00264.1.

Krehbiel, P. R., R. J. Thomas, W. Rison, T. Hamlin, J. Harlin, and M. Davis (2000), GPS-based mapping system reveals lightning inside storms, *Eos Trans. AGU*, *81*(3), 21–25, doi:10.1029/00EO00014.

Kuhlman, K. M., C. L. Ziegler, E. R. Mansell, D. R. MacGorman, and J. M. Straka (2006), Numerically simulated electrification and lightning of the 29 June 2000 STEPS supercell storm, *Mon. Weather Rev.*, *134*(10), 2734–2757, doi:10.1175/MWR3217.1.

Lakshmanan, V., T. Smith, G. Stumpf, and K. Hondl (2007), The Warning Decision Support System–Integrated Information, *Weather Forecast.*, *22*(3), 596–612, doi:10.1175/WAF1009.1.

Ledoux, H., and C. Gold (2005), An efficient natural neighbour interpolation algorithm for geoscientific modeling, in *Developments in Spatial Data Handling: 11th International Symposium on Spatial Data Handling*, edited by P. F. Fisher, pp. 97–108 , Springer, Berlin.

Lemon, L. R., and C. A. Doswell (1979), Severe thunderstorm evolution and mesocyclone structure as related to tornadogenesis, *Mon. Weather Rev.*, *107*(9), 1184–1197, doi:10.1175/1520-0493(1979)107<1184:STEAMS>2.0.CO;2.

Lund, N. R., D. R. MacGorman, T. J. Schuur, M. I. Biggerstaff, and W. D. Rust (2009), Relationships between lightning location and polarimetric radar signatures in a small mesoscale convective system, *Mon. Weather Rev.*, *137*(12), 4151–4170, doi:10.1175/2009MWR2860.1.

MacGorman, D., and Warning R & D Division (WRDD), National Severe Storms Laboratory, NOAA (2013), Oklahoma Lightning Mapping Array (OKLMA) Data, version 1.0, UCAR/NCAR - Earth Obs. Lab. [Available at http://data.eol.ucar.edu/dataset/353.089, Accessed 10 Jan 2014.]

MacGorman, D. R., and W. D. Rust (1998), *The Electrical Nature of Storms*, Oxford Univ. Press, New York.

MacGorman, D. R., W. D. Rust, P. Krehbiel, W. Rison, E. Bruning, and K. Wiens (2005), The electrical structure of two supercell storms during STEPS, *Mon. Weather Rev.*, *133*(9), 2583–2607, doi:10.1175/MWR2994.1.

MacGorman, D. R., et al. (2008), TELEX: The Thunderstorm Electrification and Lightning Experiment, *Bull. Am. Meteorol. Soc.*, *89*(7), 997–1013, doi:10.1175/2007BAMS2352.1.

Mansell, E. (2014), Mobile National Severe Storms Laboratory (NSSL) NOAA NOXP Radar Data in DORADE format, version 1.0, UCAR/NCAR - Earth Obs. Lab. [Available at http://data.eol.ucar.edu/dataset/353.215, Accessed 2 Oct. 2013.]

Mansell, E. R., D. R. MacGorman, C. L. Ziegler, and J. M. Straka (2002), Simulated three-dimensional branched lightning in a numerical thunderstorm model, *J. Geophys. Res.*, *107*(D9), 4075, doi:10.1029/2000JD000244.

Markowski, P., Y. Richardson, E. Rasmussen, J. Straka, R. Davies-Jones, and R. J. Trapp (2008), Vortex lines within low-level mesocyclones obtained from pseudo-dual-Doppler radar observations, *Mon. Weather Rev.*, *136*(9), 3513–3535, doi:10.1175/2008MWR2315.1.

Markowski, P. M. (2002), Hook echoes and rear-flank downdrafts: A review, *Mon. Weather Rev.*, *130*(4), 852–876, doi:10.1175/1520-0493(2002)130<0852:HEARFD>2.0.CO;2.

NCDC (2012), *Storm Data*, vol. 54, No. 5, 598 pp., Natl. Clim. Data Cent., Asheville, N. C.

Payne, C. D., T. J. Schuur, D. R. MacGorman, M. I. Biggerstaff, K. M. Kuhlman, and W. D. Rust (2010), Polarimetric and electrical characteristics of a lightning ring in a supercell storm, *Mon. Weather Rev.*, *138*(6), 2405–2425, doi:10.1175/2009MWR3210.1.

Potvin, C. K., L. J. Wicker, and A. Shapiro (2012), Assessing errors in variational dual-Doppler wind syntheses of supercell thunderstorms observed by storm-scale mobile radars, *J. Atmos. Oceanic Technol.*, *29*(8), 1009–1025, doi:10.1175/JTECH-D-11-00177.1.

Pruppacher, H. R., and J. D. Klett (1978), *Microphysics of Clouds and Precipitation*, 714 pp., D. Reidel, London.

Rison, W., R. J. Thomas, P. R. Krehbiel, T. Hamlin, and J. Harlin (1999), A GPS-based three-dimensional lightning mapping system: Initial observations in central New Mexico, *Geophys. Res. Lett.*, *26*, 3573–3576, doi:10.1029/1999GL010856.

Rutledge, S. A., and P. Hobbs (1983), The mesoscale and microscale structure and organization of clouds and precipitation in midlatitude cyclones. VIII: A model for the "seeder-feeder" process in warm-frontal rainbands, *J. Atmos. Sci.*, *40*(5), 1185–1206, doi:10.1175/1520-0469(1983)040<1185:TMAMSA>2.0.CO;2.

Stossmeister, G. (2012), NLDN lightning data, version 1.0, UCAR/NCAR - Earth Obs. Lab. [Available at http://data.eol.ucar.edu/dataset/353.004, Accessed 10 Jan 2014.]

Straka, J. M., D. S. Zrnić, and A. V. Ryzhkov (2000), Bulk hydrometeor classification and quantification using polarimetric radar data: Synthesis of relations, *J. Appl. Meteorol.*, *39*(8), 1341–1372, doi:10.1175/1520-0450(2000)039<1341:BHCAQU>2.0.CO;2.

Takahashi, T., and K. Miyawaki (2002), Reexamination of riming electrification in a wind tunnel, *J. Atmos. Sci.*, *59*(5), 1018–1025, doi:10.1175/1520-0469(2002)059<1018:ROREIA>2.0.CO;2.

Tessendorf, S. A., S. A. Rutledge, and K. C. Wiens (2007), Radar and lightning observations of normal and inverted polarity multicellular storms from STEPS, *Mon. Weather Rev.*, *135*(11), 3682–3706, doi:10.1175/2007MWR1954.1.

Thomas, R. J., P. R. Krehbiel, W. Rison, S. J. Hunyady, W. P. Winn, T. Hamlin, and J. Harlin (2004), Accuracy of the Lightning Mapping Array, *J. Geophys. Res.*, *109*, D14207, doi:10.1029/2004JD004549.

Waugh, S. M. (2016), A balloon-borne particle size, imaging, and velocity probe for in situ microphysical measurements, Dissertation, 189 pp., Univ. of Oklahoma. [Available at https://shareok.org/handle/11244/45407.]

Waugh, S. M., C. L. Ziegler, D. R. MacGorman, S. E. Fredrickson, D. W. Kennedy, and W. D. Rust (2015), A balloonborne particle size, imaging, and velocity probe for in situ microphysical measurements, *J. Atmos. Oceanic Technol.*, *32*(9), 1562–1580, doi:10.1175/JTECH-D-14-00216.1.

Weiss, S. A., D. R. MacGorman, and K. M. Calhoun (2012), Lightning in the anvils of supercell thunderstorms, *Mon. Weather Rev.*, *140*(7), 2064–2079, doi:10.1175/MWR-D-11-00312.1.

Westcott, N. E., and P. C. Kennedy (1989), Cell development and merger in an Illinois thunderstorm observed by Doppler radar, *J. Atmos. Sci.*, *46*(1), 117–131, doi:10.1175/1520-0469(1989)046<0117:CDAMIA>2.0.CO;2.

Wiens, K. C., S. A. Rutledge, and S. A. Tessendorf (2005), The 29 June 2000 supercell observed during STEPS. Part II: Lightning and charge structure, *J. Atmos. Sci.*, *62*(12), 4151–4177, doi:10.1175/JAS3615.1.

Yang, Q., et al. (2015), Aerosol transport and wet scavenging in deep convective clouds: A case study and model evaluation using a multiple passive tracer analysis approach, *J. Geophys. Res. Atmos.*, *120*, 8448–8468, doi:10.1002/2015JD023647.

Ziegler, C. L. (2013c), NSSL MGAUS Oklahoma-Texas Sounding Data, version 1.0, UCAR/NCAR - Earth Ob. Lab. [Available at http://data.eol.ucar.edu/dataset/353.105, Accessed 06 Jun 2014.]

Ziegler, C. L. (1985), Retrieval of thermal and microphysical variables in observed convective storms. Part 1: Model development and preliminary testing, *J. Atmos. Sci.*, *42*(14), 1487–1509, doi:10.1175/1520-0469(1985)042<1487:ROTAMV>2.0.CO;2.

Ziegler, C. L. (1988), Retrieval of thermal and microphysical variables in observed convective storms. Part II: Sensitivity of cloud processes to variation of the microphysical parameterization, *J. Atmos. Sci.*, *45*(6), 1072–1090, doi:10.1175/1520-0469(1988)045<1072:ROTAMV>2.0.CO;2.

Ziegler, C. L. (2013a), A diabatic Lagrangian technique for the analysis of convective storms. Part I: Description and validation via an Observing System Simulation Experiment, *J. Atmos. Oceanic Technol.*, *30*(10), 2248–2265, doi:10.1175/JTECH-D-12-00194.1.

Ziegler, C. L. (2013b), A diabatic Lagrangian technique for the analysis of convective storms. Part II: Application to a radar-observed storm, *J. Atmos. Oceanic Technol.*, *30*(10), 2266–2280, doi:10.1175/JTECH-D-13-00036.1.

Ziegler, C. L., and D. R. MacGorman (1994), Observed lightning morphology relative to modeled space charge and electric field distributions in a tornadic storm, *J. Atmos. Sci.*, *51*(6), 833–851, doi:10.1175/1520-0469(1994)051<0833:OLMRTM>2.0.CO;2.

Ziegler, C. L., P. S. Ray, and N. C. Knight (1983), Hail growth in an Oklahoma multicell storm, *J. Atmos. Sci.*, *40*(7), 1768–1791, doi:10.1175/1520-0469(1983)040<1768:HGIAOM>2.0.CO;2.

Ziegler, C. L., E. R. Mansell, J. M. Straka, D. R. MacGorman, and D. W. Burgess (2010), The impact of spatial variations of low-level stability on the life cycle of a simulated supercell storm, *Mon. Weather Rev.*, *138*(5), 1738–1766, doi:10.1175/2009MWR3010.1.

Ziegler, C.L., E. R. Mansell, K. M. Calhoun, and D. R. MacGorman (2014), Impact of kinematics, microphysics, and electrification on the formation of lightning-weak holes in a simulated supercell storm, paper presented at XVth International Conference on Atmospheric Electricity, Norman, Okla. [Available at http://www.nssl.noaa.gov/users/mansell/icae2014/preprints/Ziegler_324.pdf.]